Container-less Solidification of Advance Engineering and High Entropy Alloys

By

Sadeeda	**Regn. No. NUST201433394BSCME99214F**
Syed Ali Raza Jafri	**Regn. No. NUST201432423BSCME99214F**
Varda Asif	**Regn. No. NUST201432663BSCME99214F**

School of Chemical and Materials Engineering (SCME)

National University of Sciences and Technology (NUST)

2018

Container-less Solidification of Advance Engineering and High Entropy Alloys

Sadeeda	**Regn. No. NUST201433394BSCME99214F**
Syed Ali Raza Jafri	**Regn. No. NUST201432423BSCME99214F**
Varda Asif	**Regn. No. NUST201432663BSCME99214F**

This report is submitted as a FYP thesis in partial fulfillment of the requirement for the degree of

(BE in Materials Engineering)

Supervisor: Dr. Ahmed Umar Munawar

Department of Materials Engineering

School of Chemical and Materials Engineering

National University of Sciences and Technology

June, 2018

Certificate

This is to certify that work in this thesis has been carried out by **Ms. Sadeeda, Ms. Varda Asif** and **Mr. Syed Ali Raza Jafri** and completed under my supervision at school of chemical and materials engineering, National University of Sciences and Technology, H-12, Islamabad, Pakistan.

Supervisor**: Dr. Ahmed Umar Munawar**
Department of Materials Engineering
School of Chemical & Materials Engineering,
National University of Sciences and
Technology, Islamabad

Co-supervisor**: Dr. Umair Manzoor**
Department of Materials Engineering
School of Chemical & Materials Engineering,
National University of Sciences and
Technology, Islamabad.

Submitted through:

HoD**: Dr. Umair Manzooor**
Department of Materials Engineering
School of Chemical & Materials Engineering,
National University of Sciences and
Technology, Islamabad

Dean**: Dr. Arshad Hussain**
Department of Materials Engineering
School of Chemical & Materials Engineering,
National University of Sciences and
Technology, Islamabad

Dedication

We dedicate this thesis to our parents, our teachers, our siblings, our partners, and our friends; people whose constant guidance and inspiration paved our path and who supported us in our best and our worst

Acknowledgement

All praise be to Almighty Allah, for bestowing on us his blessings to help us in the completion of this work

Our sincerest gratitude to our supervisor and mentor Dr. Ahmed Umer Munawar, whose trust, training, and guidance helped us in completing our project

We would like to extend our gratitude to our Co Supervisor Dr. Umair Manzoor for his constant support throughout

We would like to thank our partners in the German Aeospace Center, Matthias Kolbe, Florian Kargl, and Mareike Wegener

We are most obliged to our instructors in the School of Chemical and Materials Engineering for helping us wherever we needed it, Dr. Aftab Akram, Dr, Khurram Yaqoob, Sir Khurram, Sir Zafar Khan, and Sir Khawar.

Our heartiest thanks to Ms. Fatima Nisar, for her diligence and for her constant support and we are also very greatful to the whole of SCME administration for providing us with the guidance we needed for the completion of our project

Abstract

Container-less solidification helps achieving large values of undercooling by totally avoiding heterogeneous nucleation at the container walls. Undercooling is nearly always required to drive the solidification front during solidification process which is the most important processing route for metals and alloys. However, heterogeneous nucleation sites tend to limit the undercooling of a melt during the solidification process by reducing the energy required to form the critical nucleus. The most dominant factor facilitating the heterogeneous nucleation and thus lowering the undercool-ability of a melt is container wall. Electromagnetic levitation (EML) is a useful technique to avoid heterogeneous nucleation due to container walls and consequently, large undercooling values can be achieved during the solidification process. Different undercooling values result in different solidification speeds which in turn determine the microstructure and mechanical properties of materials. A high-speed video camera with frame rate of 7000pictures/ second has been utilized to observe the recalescence behaviour and to calculate the solidification velocity.

This thesis includes results for the container-less solidification of hyper-eutectic NiSn and NiCoCrFe-Cu based high entropy alloys (HEAs); and its effect on microstructure and mechanical properties. Both these alloy systems are extensively studied because of their promising properties. Eutectic alloys show lower melting points than the pure elements and zero temperature range which makes them ideal for casting processes. Similarly, HEAs allow very good control over the properties by minor adjustments in composition.

It has been observed that the solidification velocity for the NiSn alloy increases with increasing undercooling. This increase is slow till a certain undercooling value is achieved where a rapid increase in the solidification velocity is observed. This is mainly due to the transition from coupled towards uncoupled growth of eutectic structure. The coupled growth results in lamellar structure which is the equilibrium structure for eutectic alloys. However, uncoupled growth results in anomalous or non-lamellar structure where one phase appears to be present in the matrix of other. In case of HEA, the microstructure consists of two-phase region. A dendritic region which is depleted in Cu forms first while the Cu-rich inter-dendritic region follows afterwards. As the undercooling increases, the Cu-rich phase tends to be segregated as spherical particles and not as continuous inter-dendritic phase.

Effect of undercooling on mechanical properties has been investigated by performing Vickers microhardness and nano-indentation tests. In case of NiSn alloy, hardness decreases with increasing undercooling. It is because inter-phase and grain boundaries, which improve the hardness, are more in lamellar than the non-lamellar microstructure. In case of HEA the undercooling increase leads to lower hardness of the alloy, the undercooled structure has less lamellar structure which results in lower hardness of the alloys because of less grain boundaries in it. For the HEAs, undercooling has been found to improve the mechanical properties. It can be attributed to the precipitate hardening due to Cu-rich precipitates which form at larger undercoolings. Nano-indentation for the HEA should be performed to understand the hardness contribution due to individual phases.

Table of Contents

Table of Figures

Chapter 1. Introduction

Undercooling is required to drive the solidification front during the solidification process. Solidification is important technique in different processes like ingot casting, continuous casting, single crystal growth, directional solidification and the most important rapid solidification of alloys that we discussed in this paper. Due to difference of undercooling values, temperature distribution, cooling rates and alloying elements, microstructure and mechanical properties differ during solidification process[1]. Information about different types of undercooling can be found from literature. A lot of researchers have studied the effect of homogeneous and heterogeneous nucleation on the solidification process which involves nucleation and growth. The container walls restrict the undercooling values by catalysing the nucleation process that promotes heterogeneous nucleation process. Heterogeneous sites tend to limit the undercooling of a melt during the solidification process by reducing the energy required to form the critical nucleus. The most dominant factor facilitating the heterogeneous nucleation and thus lowering the undercooling values of a melt are container walls. To avoid this and to achieve high undercooling values at slow cooling rates, can use container-less solidification techniques[2].

There are many container-less solidification techniques which are commonly employed like Electromagnetic Levitation Technique (EML), drop tube solidification, electro-static levitation (ESL) and aero-dynamic levitation (ADL) [3, 4]. By using different solidification techniques the microstructure and growth kinetics will be different[5-7]. Electromagnetic levitation (EML) is a useful technique to avoid heterogeneous nucleation due to container walls. In this way, large undercooling values can be achieved during the solidification process. At lower undercooling values, the solidification rate is low and the resulting microstructure is near to equilibrium. However, rapid solidification allows in-depth investigations on solidification kinetics, metastable phases, extended solid solutions and refined micro[i]structures. Abundant literature is available on studies of eutectic alloys. As the undercooling increases, the solidification microstructures of

eutectic alloys may change from lamellar two-phase distribution into a "anomalous microstructure", which appears to consist of a particulate distribution of one phase distributed in the matrix of another phase[8-11].

In order to obtain a deeper understanding of the solidification mechanisms of undercooled of hyper-eutectic NiSn alloys and to confirm the proposed mechanisms, further studies are needed. In this paper tried to manipulate mechanical properties from undercooling values and resulting solidification speed. In the present work, solidification of undercooled hyper- eutectic Ni-Sn alloy has been studied, with emphasis on the evolution of microstructure and mechanical properties as a result of undercooling. It has been observed that the solidification speed increases with increasing undercooling. This also results in a transition from lamellar to non-lamellar microstructure.
Solidified microstructures has been investigated by characterization techniques X-Ray Diffraction (XRD) and Scanning electron microscopy (SEM). Trend of hardness for different undercooling values is investigated by micro vickers and nano indentation techniques.

This thesis includes preliminary results for the container-less solidification of eutectic and high entropy alloys (HEAs). Both these alloy systems are extensively studied because of their promising properties. Eutectic alloys show lower melting points than the pure elements and zero temperature range which makes them ideal for casting processes [12]. In case of HEAs, four or more elements are added in equi or near equi-molar amounts which results in high configurational entropy, thus stabilizing the solid solution phase. Abundant literature is available on both eutectic and HEAs e.g. [12-15]. Solidification of binary eutectic alloys involves cooperative growth of two solid phases from the liquid phase. However as the undercooling during the solidification process increases, the solidification microstructures of eutectic alloys may change from well aligned two-phase distribution into an “anomalous eutectic microstructure”[16, 17]. This anomalous structure appears to consist of one phase distributed in the matrix of the other phase. For the HEAs, undercooling has been found to improve the mechanical properties [18]. Liquid phase separation has also been observed when an undercooled NiCoCrFeCu HEA is solidified using glass fluxing method [19].

A eutectic dendrite as described by Gao et al. [10] was proposed as one of the key mechanisms for the development of the anomalous eutectic, but could not be observed in this work. Therefore, for further analysis of this eutectic dendrite, atomization of the eutectic alloy should be done. As a result, very high cooling rates are achieved in small droplets, so that the eutectic dendrite may possibly be observed directly.

NiSn and HEA experiments on the electrostatic levitator (ESL) are performed. The sample is held in this levitator by a magnetic field, but melted without contact by a laser. This results in less convection in the sample, which changes the heat and mass transport before the dendrite tip. Another focus must be on determining the high temperature phase of the Ni3Sn phase to properly determine the crystal geometry. For this an in structural analysis by means of neutron or X-ray scattering is proposed.

To be able to differentiate the solidification processes in the eutectic samples for high undercoolings more clearly, separate investigations should be made on the two phases involved. Photographs of the individual solidification front and the rates as a function of the supercooling for the pure Ni3Sn intermetallic phase and the pure nickel-rich phase could help in assigning the present results to one or the other phase for high undercooling. Due to the high variability in the crystal growth rates and the different structures of the solidification front, it is conceivable that the two phases involved can individually influence the solidification process. However, this is not comprehensible without measurements of the pure phases.

Chapter 2. Literature review

2.1 Basics of thermodynamics

Thermodynamics deals with the heat changes in systems. Here we consider the solidification process to be a system dissipating heat at various rates depending upon the undercooling provided. We deal with the Gibbs Free energy that is known to be the maximum amount of work, in terms of heat, that can be obtained from a closed system. A state of matter that has a lower Gibbs free energy at a given temperature has more probability to exist at that point. This helps us study the speed of solidification and the movement of the liquid – solid interface in solidifying material with respect to the solidification temperature or provided undercooling temperature.

The phase transition occurs when there is a considerable difference in the Gibbs energy of the two phases, the overall process leans towards the phase with lesser Gibbs energy. Although, the formation of solid-liquid interface during solidification causes an increase in the Gibbs free energy (The Gibbs Thomson Effect), the overall energy of the system decrease (making it stable) when it solidifies at lower temperatures.

The increase in Gibbs free energy contributed by the interfacial energy of solid – liquid interfaces is the reason liquid is held between the solidified particles in its metastable form for an indefinite amount of time, even at lower temperatures[20].

2.2 Solidification

Solidification refers to the state change in metals and their alloys from liquid to solid, which is accompanied by the emission of considerable amount of heat. This lead to the formation of a crystalline structure. Crystalline structure is formed by the help of two processes; nucleation of the solid phase followed by the growth of nucleus to crystal. The first process consists of forming nuclei in the melt

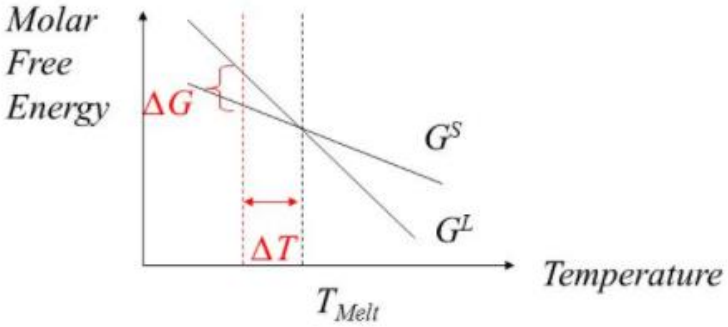

Figure 1. Driving Force for Solidification

while the second consists of how fast the nuclei grow, which is also known as the crystallization speed.

The solidification happens only if the Gibbs energy of that material in solid state is lower than the gibbs energy of the material in liquid state. This relation exists below the melting temperature or the transition temperature of the metal. Under equilibrium conditions, at the transition temperature, the gibbs energy of both the states is equal and the metal exists in both forms[21]. To start solidification further from this point, some amount of undercooling is required which provides the driving force for solidification.

2.3 Nucleation

Nucleation can be defined as the initial process that needs to occur in order to form a crystal. A nucleus leads to the self-organization of atoms in a melt that come closer to release energy and become small starting points for the solidification of the material.

Nucleation is generally categorized as homogenous and heterogenous. In the former, the atoms tend to come closer, in correct order, while randomly moving through the melt. While in the latter, the surface of a different material, or some particle of impurity in the melt initiated the process by having atoms or molecules gather around it in an orderly manner.

Practically speaking, the heterogenous nucleation has more chances to occur as compared to homogenous nucleation as it requires either supersaturation or a large amount of undercooling[21, 22].

2.3.1 Homogenous Nucleation:

As the solidification front moves forward in the melt, it leaves behind a arrangement of crystals, these are known as nuclie. Nuclie are the starting point for solidification and can be used for a rapid transformation in a supercooled melt. This kind of solidification occurs in homogenous nucleation system where the resulting microstructure is of only one phase. This phenome is further explained by the volmer and weber model.

The nuclei form at the material's melting point below which, further growth of the nuclei or solidification of the melt begins. This process is described as metastable state of the system where the nuclei forms a spherical shape with an interface between the liquid and the solid

phase. The formation of the interface brings a change in the overall gibbs free energy of the system. The change is can be mathematical represented as,

Free Energy (Area)

$$\Delta G_A(r) = 4\pi r^2 \gamma$$

And

$$\Delta G_V(r) = -\frac{4}{3}\pi r^3 \cdot \Delta g_{SL}$$

Free Energy (Volume)

The total free energy of the system is obtained by added the above-mentioned energies.

$$\Delta G(r) = \Delta G_V(r) + \Delta G_A(r) = -\frac{4}{3}\pi r^3 \cdot \Delta g_{LS} + 4\pi r^2 \gamma$$

Furthermore, Δg_{LS} is called the free crystallization energy per molar volume. This is the energy that is present of the surface of the solid liquid interface. $\Delta g_{LS} = \frac{\Delta G_{LS}}{V_{mol}}$

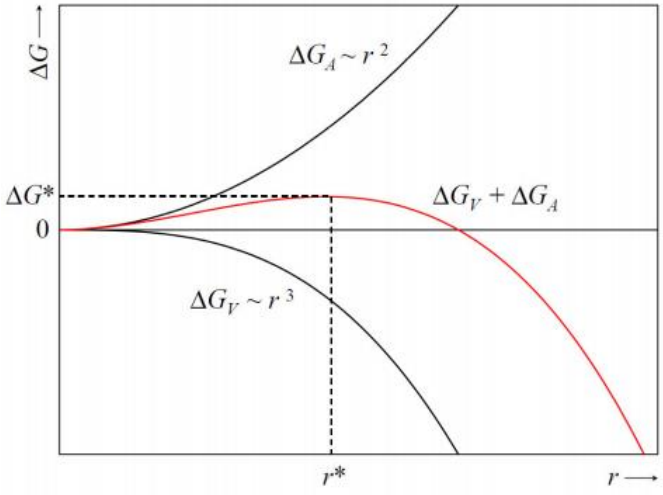

Figure 2. Gibbs Free Energy vs. Radius. shows how the free Gibbs energy G changes with increasing nuclei radius, r * is a critical germinal radius when ΔG < 0, grows a stable nuclei and the melt solidifies.

The activation energy of the homogenous nucleation can be derived by using the above mentioned equations to be,

$$\Delta G^{*}_{hom} = \frac{16\pi}{3}\frac{\gamma^3}{(\Delta g_{LS})^2}$$

Where r * is called the critical radius, minimum radius of a nuclei to start crystal gowth.

2.3.2 Heterogenous Undercooling:

In practical experiments, homogenous nucleation does not occur. This happenes due to the presence of impurities or other phase, heterogenous nucleation tend to happen more easily. In this type of nucleation, the walls of the crucible and the impurities present in the melt help start the nucleation process. This factor reduces the activation energy of heterogenous nucleation as it takes the driving force of it movement from the walls and not on its own. this is the reason why in heterogenous nucleation, the solidification front tends to move forward rapidly as compared to homogenous nucleation. The activation energy of the heterogeneous nucleation ΔG(het) is dependent on the activation energy of the homogeneous nucleation ΔG(hom)and$f(\theta)$;

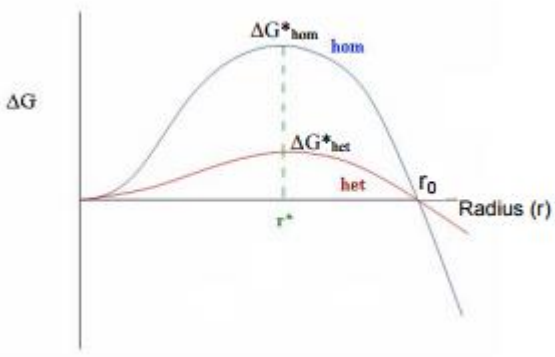

Figure 3. Heterogeneous and Homogenous Nucleation

$$\Delta G_{het} = \Delta G_{hom} \cdot f(\theta)$$

Considering the critical nuclei radius, the heterogeneous nuclei formation is the same as in homogeneous formation but the structural factor $f(\theta)$ be taken into account additionally with heterogenous nucleation and volume is also less for heterogeneous nucleation.

$$r^* = -\frac{2\gamma_{\alpha\beta}}{\Delta G_r}$$

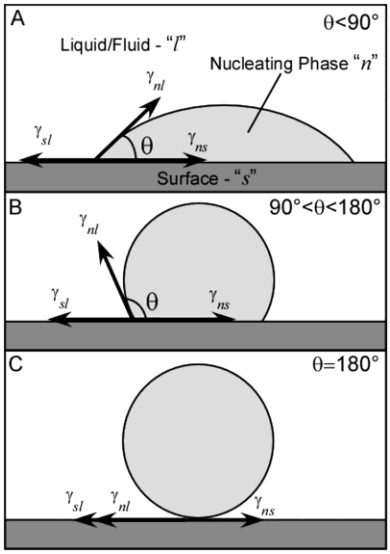

Figure 4. Nucleation Depending on Surfaces

The structure factor $f(\theta)$ describes the catalytic effect on the nucleation process and is as follows:

$$f(\theta) = \frac{2-3\cdot\cos\theta+\cos^3\theta}{4}$$

$f(\theta)$depends on the wetting angle of the melt and the foreign phase and varies between zero and one.

At $\theta = 180°$ no wetting takes place, so that this nucleation case is equivalent to the homogeneous one. For an angle of $f(\theta) = 0$, complete wetting takes place.
Heterogeneous nucleation can therefore be easier than homogeneous nucleation as energy needed is reduced in this case, depending on the wetting angle. Wetting angle describes the ease of nucleation. Therefore, it is necessary to reduce the number of critical nucleas to provide for poor wetting of the germinal surface[23].

2.4 Undercooling

Undercooling is discussed as the process of lowering the temperature of the melt below its transition temperature without obtaining a state change. Undercooling plays as important role when it comes to solidification, as it provides the force that drives the liquid solid interface forward in the melt aiding the solidification of the melt. The change is amount of undercooling controls the rate of solidification, the velocity of crystal growth and the final microstructure. The microstructure, which is altered by the provided undercooling exhibits various properties that can prove to be useful in many applications[24].

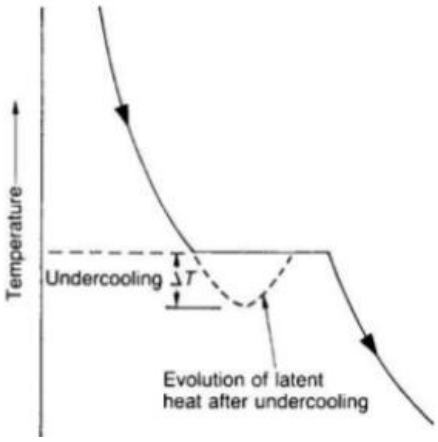

Figure 5 Cooling curve for a pure metal showing possible undercooling

2.5 Eutectic alloys solidification

A eutectic alloy, is the mixture of two metals at a fixed composition where an equilibrium cooling and solidification rate gives a lamellar structure or rods of minor phase embedded in the major phase matrix.

Eutectic solidification of an alloy results into two solid phases that can be differentiated by the amount of solute concentration present in them. The arrangement of these two phases can vary which solely depends upon the type of alloy system under observation. These arrangements form during equilibrium or near equilibrium cooling conditions and are visible as contrasting layers under a microscope

The solidification process results in a two-phase layered structure formed directly from a homogenous melt. The process started when alpha phase starts solidifying leaving the melt rich in beta phase. The melt, in the effort to return to its equilibrium concentration, starts diffusing beta phase out of the melt. This process keeps on progressing until an alternating layered structure is achieved in the final step[25].

2.6 Hyper Eutectic Solidification

Hyper eutectic composition lies ahead of the eutectic composition in a phase diagram. The microstructures obtained show parts of eutectic structures formed in the alloy along with an abundance of one of the two phases.

Here, when a hypereutectic solidification starts, the beta phase starts nucleating first due its abundance in the melt. When the sample reaches its transition temperature, all the extra beta is already diffused out and the rest of the melt has near eutectic composition. In the final step, the

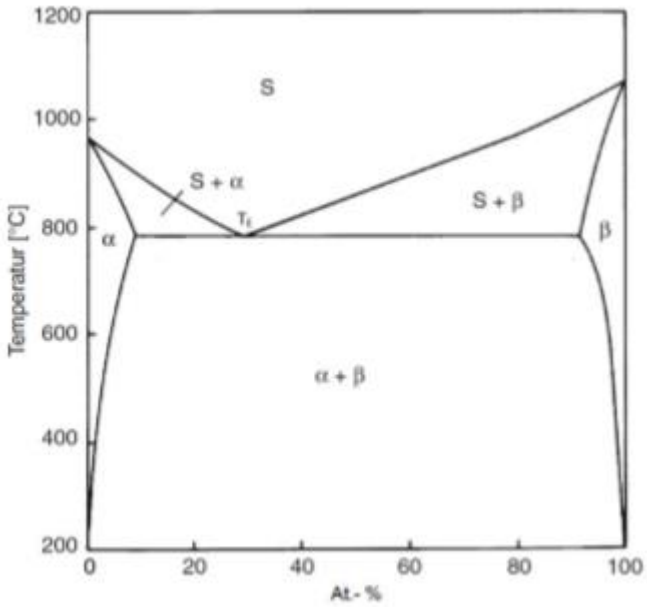

Figure 6 Schematic representation of a eutectic phase diagram. The phase α, β and melt (S) are in equilibrium at the eutectic point.

microstructure consists of beta phase grains mixed with alternating layered structure of eutectic composition. [26]

2.7 Theory OF Nickel Tin Alloy (NiSn)

During solidification, there are structural changes that occur inside the alloys. These structure changes occur because of the undercooling that is the result of the rapid cooling during the solidification process. Different undercooling values have different effects on the dendrite growth of the undercooled alloy. When the temperature gradient achieved during undercooling is small, the resultant microstructure has coarse grains along with bigger tipped dendrites, on the other hand when the value of the temperature gradient achieved during undercooling is large; the resultant microstructure has a more fine structure and small dendrites. The dendrites formed in the fine microstructure have smaller tips that suggest the presence of high crystal growth velocity of the sample.

The dendrites that are formed with high values of undercooling have more coherent tips. This indicates that the sample material experienced a uniform rate of solidification. This allows the dendrites to form a more logical structure. This however is not observed in the samples that went undercooling of lower values. This proves that in this process, multiple solidification fronts are present that lead to this incoherency. At lower undercoolings, more time is required for recalescence to occur, however for higher undercoolings, less time is required for the same process to occur[5].

During the process of solidification, the undercooling in the sample disperses with the primary dendrites thickening. When the value of undercooling is high, a fine structure of the dendrite arms occurs because of the increased space between the dendritic arms. The rapid recalescence occurs when the liquid melt is no longer undercooled with respect to the solid dendrite arms. The coarsening occurs after the temperature t_r is achieved therefore the recalescence occurs at a slower rate.

The dendrite arm that contains more solute tends to melt first when the recalescence occurs. In lower values of undercooling, the solute does not get enough time to distribute itself efficiently. This results in a high contrast in the dendrite arms which is easily visible. This leads to the solute

not integrating well with the structure at lower undercooling. The poor cores in the dendrite arms lead to a huge contrast which is clearly observable.

As the microstructure becomes finer when the undercooling is increased, the conventional branched dendrite arms tend to arrange themselves in spherical patterns and the end microstructure achieved is aided by the ripening phenomena. The solidification in the centre is slower as compared to the surface of the sample. At increased undercoolings, the minimum amount of solute concentration in the dendrites increases to a concentration where the stability of the structure is maximum[6].

When the composition of the sample material is eutectic, the shrinkage of the intermetallic liquid is rapidly removed so the ripening that occurs is very limited. The structure however becomes lamellar after the eutectic point. The amount of the lamellar structure achieved decreases with the increase in undercooling.

The dendrite growth rate of Fe based multinary alloys was observed to be slow for low undercooling values between the ranges of 67 K and 250 K. Once the temperature exceeds 250 K however, the velocity of the crystal growth was observed to increase drastically at 3 m/s. This dendrite growth velocity is a very important factor in determining the mechanical properties of the alloy as they have a considerably large effect on them. An increase in the velocity also resulted in an increase in the alloy hardness. The trend can be divided in to two parts:

i. The drastic increment in hardness as velocity rises from 0.02 to 8 m/s.
ii. The slower increase in hardness as velocity increase from 8 m/s till 31.8 m/s

The cause for the variations in the mechanical behavior is because of the formation of the refined grains along with the changes in the microstructure which are produced because of higher dendrite growth. This increased dendritic growth leads to changes in the grain size, and tells us what the microhardness of the alloy is due to dendritic growth velocity[7].

2.7.1 Dual origin of anomalous eutectic structure in undercooling

The recalescence front observed during the process can help us in measuring the crystal growth velocities. The total distance travelled by the recalescence front when divided by the total time required for the solidification of the sample, gives us the total growth velocity of the sample. The crystal growth velocity increases non-linearly with the increase in the undercooling. When the undercooling value is intermediate, a sudden rise in the growth velocities can be recorded.

This increase in velocity can be attributed to the formation of anomalous eutectic structures inside the sample material rather than the coupled eutectic growth. The coupled eutectic growth needs diffusion to occur between phases. This is a comparatively slower process, then the formation of the anomalous eutectic phase. The anomalous phase formed consists of various grain sizes and orientations of the Ni rich phase since this phase is not achieved in equilibrium conditions.

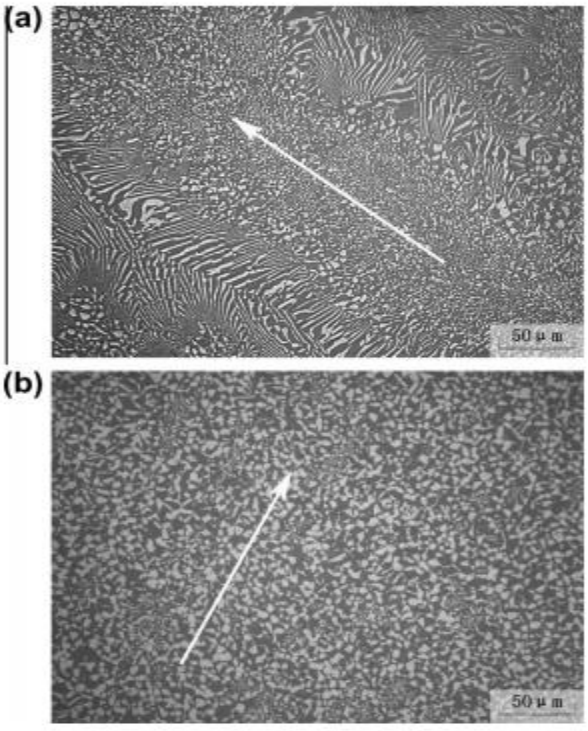

Figure 7 Micrographs of microstructure of glass-fluxed Ni–Sn with different undercoolings. (a) Regular lamellar eutectic and anomalous eutectic for DT = 40 K. (b) Coarse-grained and fine-grained anomalous eutectic bands for DT = 202 K

At low undercooling values, the anomalous structure is produced by eutectic dendrites whereas at high values of undercooling, the anomalous structure is produced by Ni rich single phase dendrites. The amount of the anomalous eutectic present in the sample's microstructure increases as the value of the undercooling increases. During the levitation process, dealing with the path of recalescence front becomes a challenge, this is because of the unbalanced and spontaneous nucleation occurring within the samples causes oscillations during the levitation.

The remelted sample experiences two recalescence fronts; the first front is observed when the liquid part in the structure loses its energy and the process for solidification is rapid. The second

front we observed was when the Ni_3Sn phase is formed in solid state. Low values of undercooling do not provide enough driving force for the dendrites to effectively move forward. This causes the front to move forward in a random path along the edges which is difficult to record or predict. At high values of undercooling however, the driving force is enough to move the dendrites forward, and a clearly visible and defined recalescence front is observed to follow to steady path across the sphere. This is the reason why the undercooled grains have directionality.

As the undercooling of the microstructure is increased, there is a difference of amount of diffusion between the grains as the front moves forward during solidification. This causes a banded microstructure which consists of coarse grained and fine grained anomalous eutectic microstructure as is shown in Figure 7. The formation of the anomalous eutectic is not directly formed from the lamellar eutectic structure, as is evidenced from the difference in the morphology. The primary dendrites melt during the recalescence and solidify rapidly to form an anomalous eutectic. This anomalous eutectic contains Ni rich grains existing in various orientations. This is because when during solidification, when heat is dissipated from various nucleating points in the melt, it passes through the entire melt due to convection of the heat energy. This results in the rotation of the grains in various directions[10].

2.8 High Entropy Alloys

High entropy alloys are defined as a mixture of at least five basic elements with equal atomic concentration of at least 5% each. The gibbs free energy of a mix depends upon the enthalpy of the mix, the temperature at which the mix is kept and the entropy of the mix. The relation can be represented as:

$$\Delta G_{Mix} = \Delta H_{Mix} - T\Delta S_{Mix}$$

The mixture of these basic elements has high value for ΔS_{Mix} which tend to stabilize the structure as compared to intermetallic compounds that normally form in binary or tertiary alloy systems. The structure of high entropy alloys enables them to be produced, machined and readjusted with respect to the application with an incredible ease. The main contribution to entropy is the due to its configuration. The change in configurational entropy per mole for making a high entropy alloy can be mathematically represented as:

$$\Delta S_{Mix} = -R \sum_{k=1}^{n} X_k \, Ln \, X_k$$

Where, R is the Universal gas constant, n is number of basic elements in a high entropy alloy sample and X is the mole fractions of the elements.

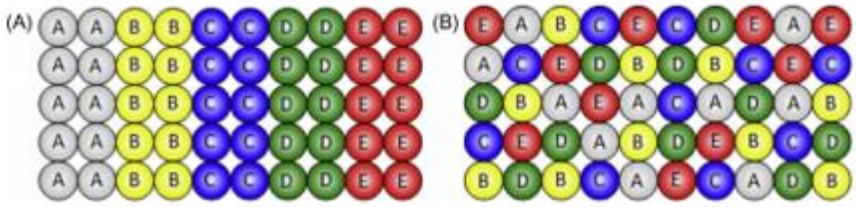

Figure 8 Figure 8 (A) Five different atoms before mixing, (B) the atoms after forming a random solid solution

2.8.1 Factors effecting HEAs

There are four major factors that may change the microstructure and properties of high entropy alloys. The factors are discussed below.

1. **High entropy effect:**

High entropy effect enables the solid solution formation and reduces the complexity of the structure. Since high entropy of the solution gives it a lower gibbs free energy making it simple and stable. Moreover, as the number of elements in the mix increase, the gibbs energy is observed to be lowered especially if the test temperature is high as well making the mix more stable. For high entropy effect to work, the elements should be thoroughly mixed to possess enough randomness in their configuration to have high entropy value.

2. **Severe Lattice Distortion Effect**

Since there is not order in the arrangement of atoms in high entropy alloys, the different types and sizes of the atom cause lattice strain. As there does not exist any pattern, the unit cell formed from all the types of atoms present in the mix does not have the same shape as its adjacent cell either. This factor decreases the influence due to temperature on the properties. It causes the mechanical properties i.e. hardness and strength to improve as distortion results in inhibition of plastic deformation.

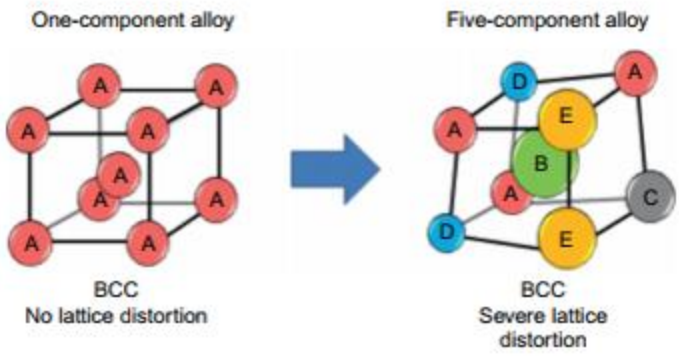

Figure 9 Lattice distortion in five-component alloy

Since the ordered planes are missing from the structure, the x ray diffraction gives smaller peaks due to high diffuse scattering of x-ray. The lattice disorder causes the electrical and thermal resistivity to increase as the electrons phonons tend to scatter respectively. Here, the atomic vibrations due to high temperature are not as dominant as the lattice distortion itself.

3. Sluggish Diffusion Effect

In order to form different phases, atoms diffuse from place to place during the transformation phase. Since high entropy alloys consist of different type of atoms in a solid solution state, if a vacancy exist in the matrix there is a higher competition between the different atoms to fill it which would decrease the amount of diffusion that occurs. Moreover, a large amount of activation energy would be needed for the movement of atoms as the distorted lattice sites have difference in their lattice potential energy. So the vacant sites with low lattice energy would attract all atoms causing a slower rate of diffusion.

Low diffusion rate influences the nucleation, crystal growth, spread and structure of the newly formed phase. This can provide a huge control of diffusion to manipulate the microstructure of the alloy in order to achieve desired properties for a specific application. A control over the diffusion rate helps in obtaining supersaturated solution with ease, fine precipitates, high temperature for recrystallization, low crystal growth velocity, less grain coarsening and high creep resistance. Thus, High entropy alloys can be mechanically enhanced with great ease. Aside

from achieving higher toughness and strength values, higher creep resistances in a part will help increase its life cycle even in harsh conditions.

4. **Cocktail Effect**

High entropy alloys, can be referred to as a cocktail of at least five principle elements which contribute to the properties exhibited by the alloys. The properties are not just from the individual element, but also from the single, dual and tertial phases they form in the alloy. This effect enables the alloy to have properties like, moderate plasticity, enhanced strength and high value of electrical conductivity. [14]

2.8.2 Nanostructure HEAs with multiple elements

The structure of an alloy made form 5 fundamental element was predicted to be complex resulting in unsuitable machining and mechanical processing, but the solid solutions were found to be simpler due to the presence of their high mixing entropies.

The solid solutions form due to the presence of higher entropies and less enthalpy with inhibits the formation of intermetallic to some extent which indicates that the structure does order itself due to the high mixing entropy. This mean that higher number of elements would result in a disordered solid solution and not in intermetallic compounds.

High entropy alloys form simpler structures that very with the mole fraction of the elements involved.

Although, high entropy alloys do undergo transformations to form multiple phases but due to the slow diffusion rate, the nucleation and growth rate are low which form very fine crystals.

High entropy alloys achieve precipitates of single crystals at nano-scale from spinodal decomposition which are otherwise obtained with additional heat treatments in conventional alloy systems. Most HAEs consist of a simple structure of precipitates embedded in a solid solution matrix.

High entropy alloys have hardness values between 130-1100 Hv. The high hardness values are obtained for the following reasons.

1. The solid solution of different type of atoms tend to impede the dislocation movement, preventing plastic deformation.
2. Precipitation hardening occurs as well due to the precipitates present in the structure at micro level.
3. Sometimes, a strong amorphous phase also exists in the structure contributing to the mechanical properties of the alloy.

High entropy alloys show a high level or resistance towards anneal softening and FCC structure HEA maintain their hardness, compressive yield strength and ductility at high temperatures as well. All these attributes make high entropy alloys better suited for high temperature applications.

High entropy alloys containing copper, titanium, chromium, nickel or cobalt tend to show resistance to corrosion.

Applications: Tools, Molds, Dies, Mechanical parts, Furnace parts

These alloys possess a high tolerance towards impurities which enables them to be produced from recycled material which is cost effective as well as an environmental advantage.[14]

2.9 Electromagnetic levitation (EML)

The formation of heterogeneous nuclei in supercool molten metals, for example when crucible walls can be avoided, this is possible if container-less solidification occur. One example of this is electromagnetic levitation (EML), which is discussed below in more detail. In addition to a very pure experimental atmosphere this offers us the advantage to detect variables by different procedures. For example, the sample temperature can be determined pyrometrically and the solidification front by means of a high-speed camera analysis.

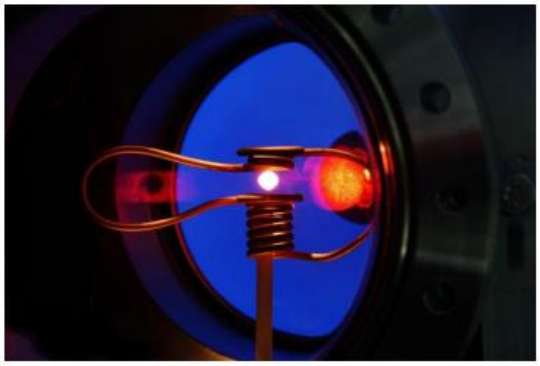

Figure 10 Melted sample in one electromagnetic levitator (EML) under Inert gas atmosphere. The upper turns the coil acts as an electromagnetic pole to stabilize the sample.

This method is based on the principle of eddy currents in an electrically conductive sample which is located in an alternating electromagnetic field. In EML sample object is suspended with

no support other than the electric and magnetic fields. These forces are used to counteract the effects of the gravitational acceleration and any other acceleration.

By means of high frequency generator an electric alternating field created, to a water-cooled copper coil which generates an electromagnetic field. This field induces Eddy currents in the sample, which leads a Lorentz Force on the sample due to the gradient of the external alternating field. For the coil geometry shown in Figure 10 the Lorentz force opposite to the gravitational pull and allows the levitation of the sample.

During levitation process the stability of sample depends on many factors like Coil design, the size of the sample and its electrical conductivity. The most stable position is reached when the sample is in the minimum potential of the field. Ohmic losses of induced eddy currents in the sample additionally cause the sample to heat up.

This principle has the disadvantage that it is not possible in most casesto cool down molten sample because of its heat radiation, as always one minimum power is induced to keep the sample in suspension. For this reason external cooling is used by blowing the sample with inert gases and cooled convectively. The principle of electromagnetic levitation is shown schematically in Figure 11.[22]

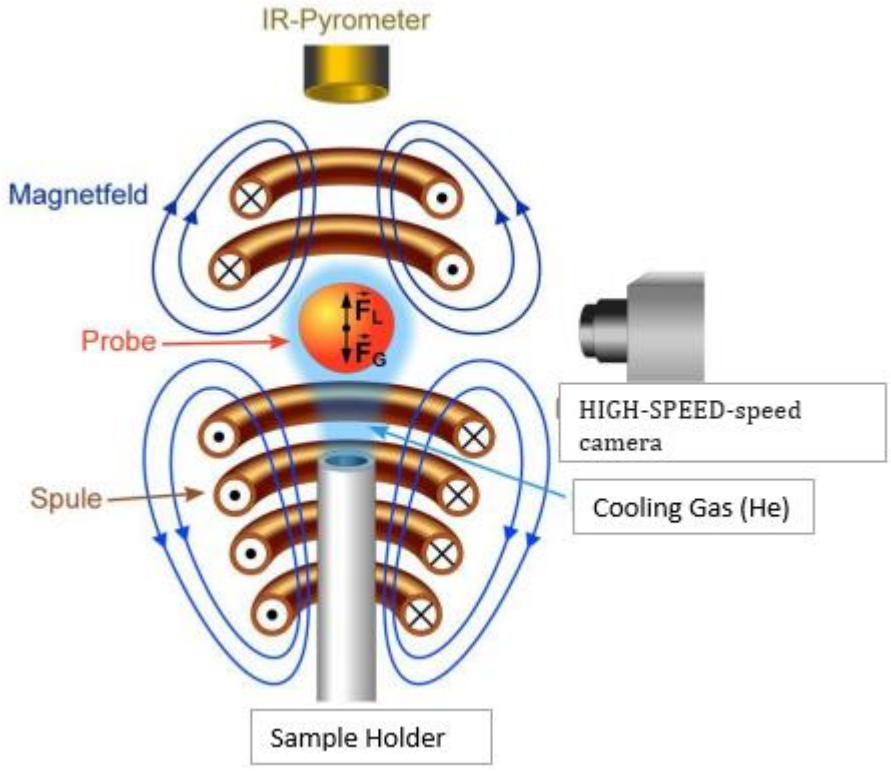

Figure 11 Schematic representation of the coil system in the EML. In addition to the forces acting on it the field lines of the adjacent electromagnetic fields are shown on the levitating sample.

2.10 Scanning Electron Microscopy:

2.10.1 Imaging

The Scanning Electron Microscope (SEM) uses electron radiation to visualize the microstructure of a sample. The electron beam is emitted at a cathode and accelerated toward the sample, where the surface of the sample to be examined is scanned in a grid. Investigations are performed under vacuum to avoid interaction of the electron beam with the molecules of the air. Typical energies of the electron beam are between 0.5 keV and 20 keV. The possible magnification depends on the diameter of the electron beam. If the focused electron beam strikes the sample, interactions with the atoms of the investigated material occur. Three main processes are distinguished:

(i) reflection of high-energy electrons by elastic scattering,
(ii) emission of secondary electrons by inelastic scattering, and
(iii) emission of electromagnetic radiation.

2.10.2 Electron backscatter diffraction:

Electron backscatter diffraction (EBSD) is used to determine the crystal structure on the surface of crystalline materials. Thus, by traversing the sample surface, modern EBSD systems can provide and graphically illustrate information about particle size distribution, grain boundaries, crystal structure and other morphological properties in a very short time. The information is derived from backscatter images (Figure 11), which are displayed on a phosphor screen. Experience shows that the best quality of the backscatter images results from a tilt angle of 70 °. Qualitatively, the backscatter images can be described as follows: The incident, monochromatic electron beam fans in the sample by inelastic scattering and thus receives a distribution in the direction of movement of the electrons. This leads to constructive interference in electrons that fulfill the Bragg relationship with the plane crowds of the crystal lattice. With knowledge of the crystal lattice, the lines occurring in the scattering image can be assigned to specific crystal

planes and the crystal orientation can be determined. This process now takes place computer-aided by analysis programs. In this way, an image of the local crystal orientation of the sample surface can be created.

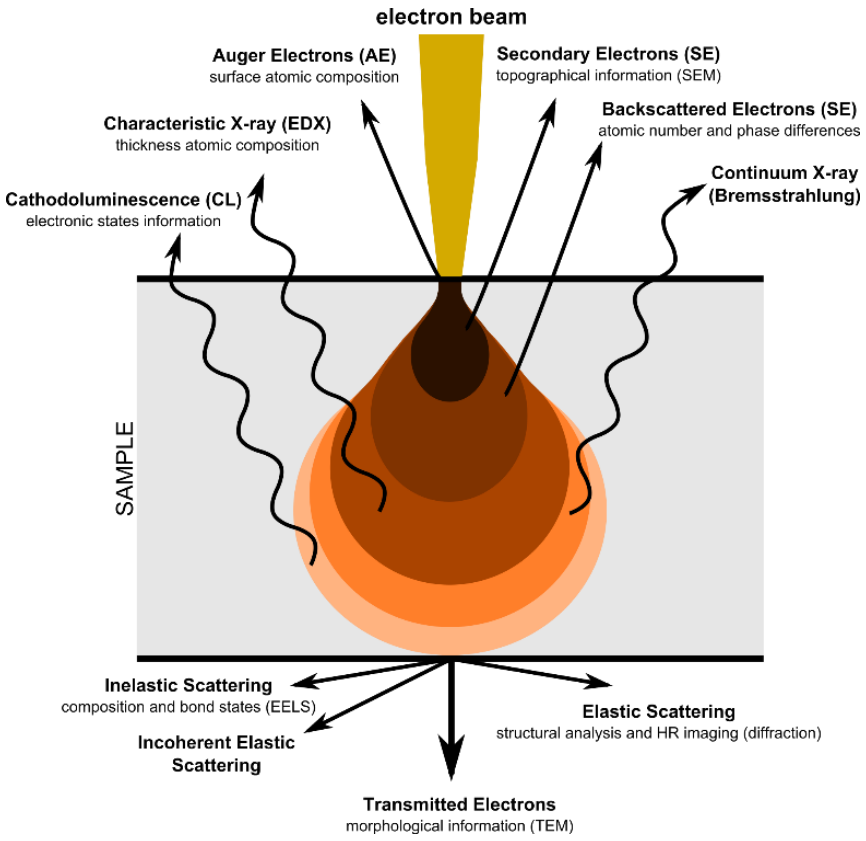

Figure 12 Scheme of the signals resulting from the interaction of the electrons and the sample.

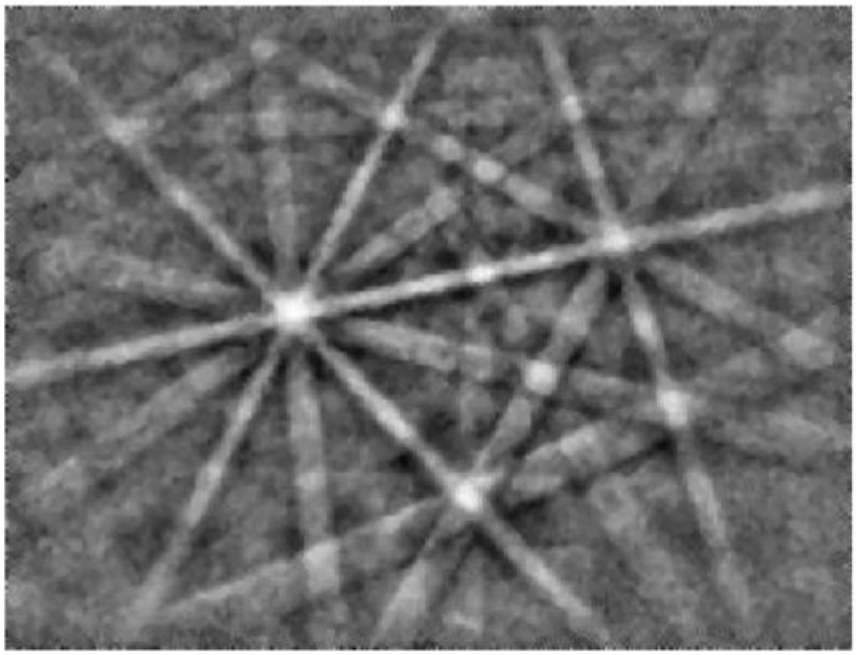

Figure 13 Taking a diffraction image

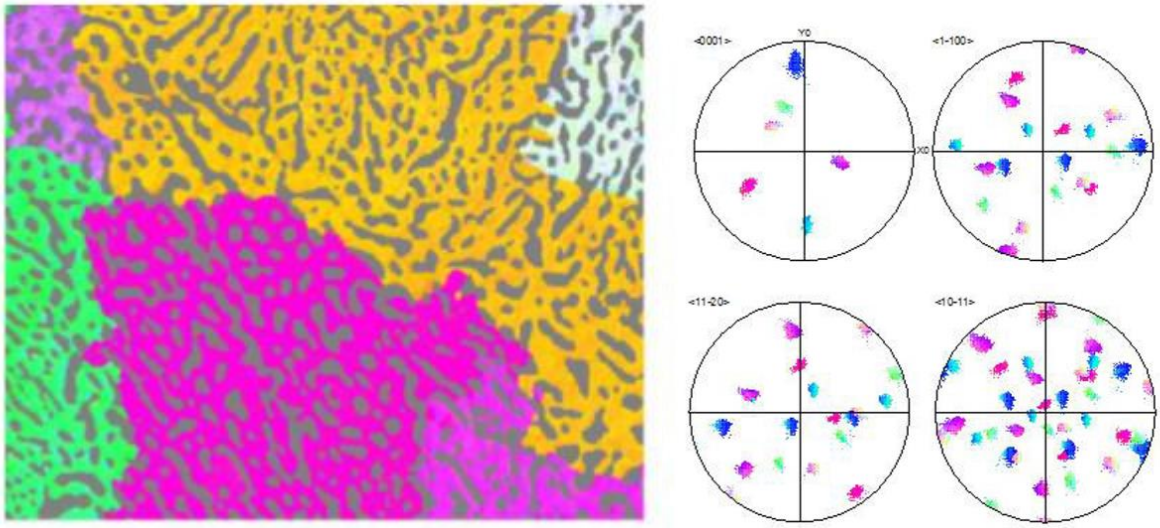

Figure 14 left: Orientation map of a Ni3Sn microstructure. The different colors represent the different orientations of the grains in the sample; right: IPF plot of the grains

The color plots for the hexagonal standard triangle and the standard cubic triangle are shown in Figures 15 and 16. In the case of the cubic crystal structure, red is assigned to the directions near the (001) corner, green to the directions near the (011), and blue near the directions of (111).

Color plot of the cubic crystal structure

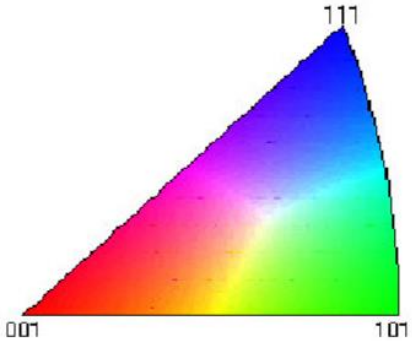

Figure 15 Color plot of the cubic crystal structure

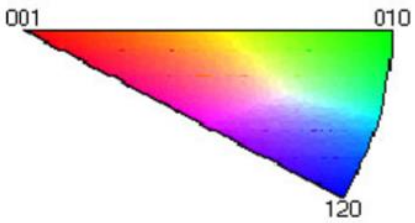

Figure 16 Color plot of the cubic crystal structure

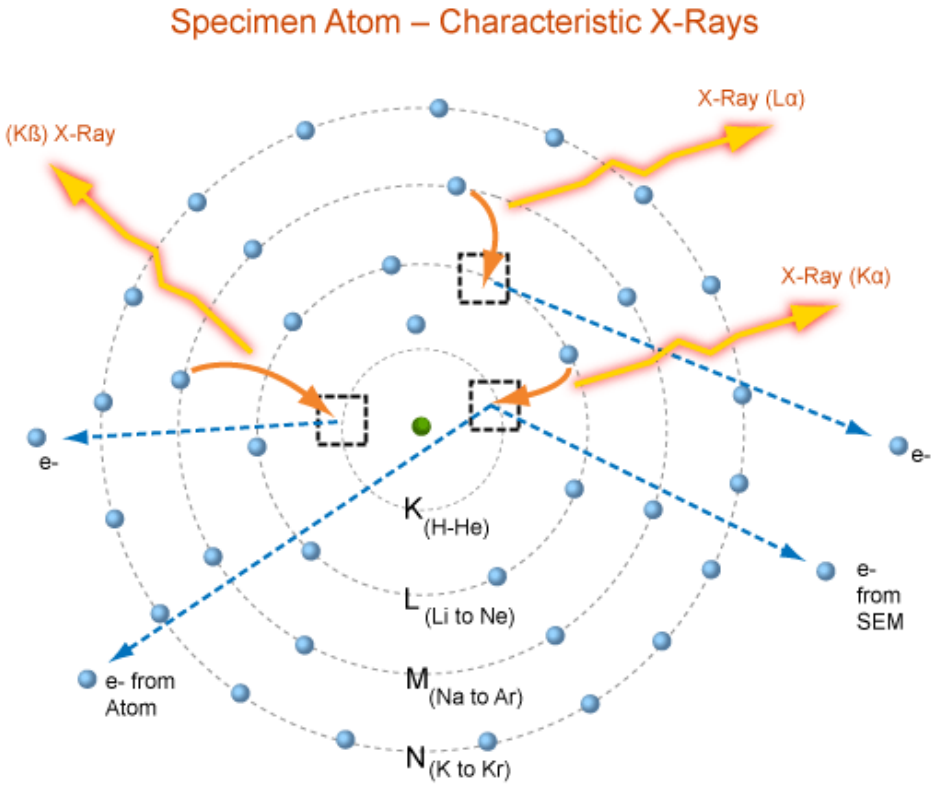

Figure 17 Color plot of the hexagonal crystal structure

Energy dispersive X-ray spectroscopy:

In the case of energy-dispersive X-ray spectroscopy (EDX) characteristic X-ray radiation is used to determine the chemical composition of a sample. Atoms of a sample are excited by a monochromatic electron beam, whereby a bound electron is beaten out of a shell. The resulting gap on the shell is immediately filled by a higher-energy electron from a higher shell. In this transition, a specific energy contribution is released in the form of an X-ray quantum. This is characteristic of a transition in the electron configuration of the atom by containing it. Different transitions are allowed for each atom, so that different X-ray quanta are emitted, depending on which energy state is "filled in". These transitions differ for the different chemical elements.

The signal intensity at the detector is plotted as a function of the energy of these X-ray quanta, for nickel and tin shown in Figure16. The different peaks for an element are assigned to the different energy transitions. The unspecific background noise is generated by Bremsstrahlung.

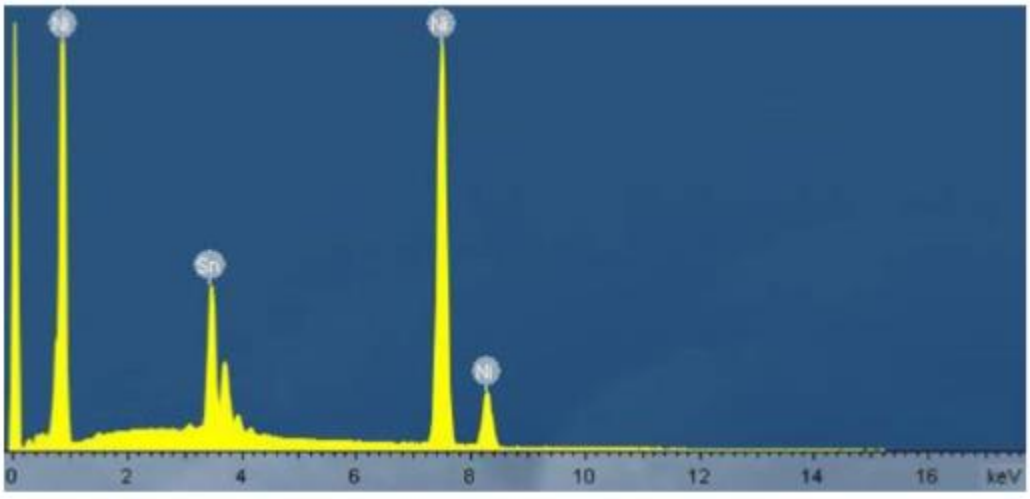

Figure 18 Energy spectra of a Ni-Sn sample. The position and intensity of the peaks can be used to deduce the chemical composition and alloy content of the individual elements in the sample.

Chapter 3. Experimental Procedures

The primary objective of the research stay in DLR was to prepare high engineering and high entropy alloys and perform the undercooling procedures on these samples. The entire process comprised of 7 steps. These are explained below in detail:

3.1 Collection of elemental samples

The first step was to take the samples in pure elemental forms which consisted of rods of elements such as Nickel and Tin for the High Engineering Alloys and Nickel, Copper, Iron, Cobalt, and Chromium for High Engineering Alloys. The purity of these samples was 99.999 %. They were fed into a semi automatic cold saw machine; the pure metal rod would be fixed into the machine and will be allowed to move perpendicularly to a rotating saw blade which helped in deciding the thickness of the resultant cut. The rotating speed of the blade can be adjusted. This is a very efficient tool to cut metals in cylindrical shape. A cold saw is a circular saw designed to cut metal which uses a toothed blade to transfer the heat generated by cutting to the chips created by the saw blade, allowing both the blade and material being cut to remain cool. Cold saws use either a solid high speed steel (HSS) or tungsten carbide-tipped, resharpenable circular saw blade. They are equipped with an electric motor and a gear reduction unit to reduce the saw blade's rotational speed while maintaining constant torque. This allows the HSS saw blade to feed at a constant rate with a very high chip load per tooth.

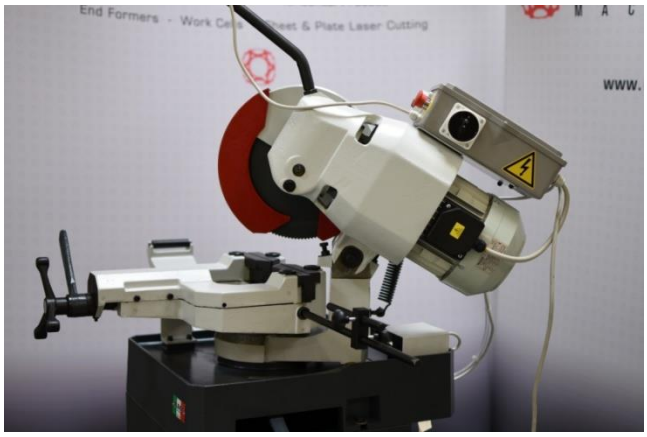

Figure 19 Automatic Cold Saw Machine

For the samples that were not in this particular shape (in our case, Nickel provided to us was not in the cylindrical form) the cutting apparatus used was a diamond wire cutter. In this apparatus, a diamond wire is wound around two simultaneously rotating wheels which slowly move forward and cut into the metal that is held in front of it. One of the rotating wheels is immersed in a cooling agent, which helps keep the wire cool and collects the cut pieces of the metal that is separated from the bulk. The metal is glued to a holding stage and is held in front of the diamond wire. The wheels move in one direction for a while and then switch to the opposite direction to avoid overheating of the wire.

3.2 Equiatomic distribution

The next step was to distribute the samples into equiatomic weights so as to get the desired representation of the metals in the resultant alloys, for this purpose, a highly sensitive weight balance was used and the metals pieces were cut into the required weights and stored in containers. The focus of the work for Nickel Tin Alloys was on the eutectic in the system nickel-tin at one composition of 83.5 at% nickel and 34.5 at% tin. In the above concentration and TE = 1130 ° C (eutectic point) are the three phases Ni, Ni3Sn and the melt in equilibrium. The nickel phase can be in the temperature range of 1130 ° C-900 ° C. The Phase diagram of the Nickel Tin diagram can be seen in the FIGURE

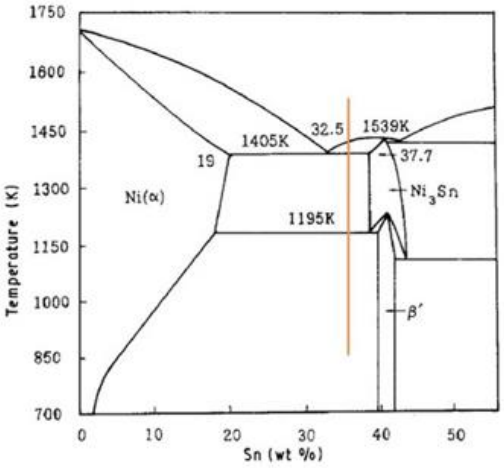

Figure 20 Revelant Portion of the Ni - Sn phase diagra

The weights of the High Entropy Alloy samples are shown below

1. High Entropy Alloy (JHC)Standard weight amounts:

Fe: 231.885 mg Cu: 263.857 mg Cr: 215.900 mg Co: 244.674 mg Ni: 243.678 mg

JHC-1:	**JHC-2:**	**JHC-3:**	**JHC-4:**
Fe: 232.286 mg	Fe: 231.714 mg	Fe: 231.020 mg	Fe: 232.408 mg
Cu: 264.036 mg	Cu: 262.986 mg	Cu: 263.838 mg	Cu: 264.030 mg
Cr: 214.480 mg	Cr: 214.102 mg	Cr: 216.732 mg	Cr: 215.850 mg
Co: 244.648 mg	Co: 244.458 mg	Co: 244.220 mg	Co: 243.666 mg
Ni: 244.934 mg	Ni: 242.932 mg	Ni: 243.864 mg	Ni: 244.194 mg

2. Advanced Engineering Alloys (MJs)

2.1. MJ FeCoNi

Standard weight amounts:

Fe: 318.69 mg Co: 336.265 mg Ni: 345.04 mg

MJ NiCoFe-1	**MJ NiCoFe-2**	**MJ NiCoFe-3**	**MJ NiCoFe-4**	**MJ NiCoFe-5**
Fe: 329.226 mg	Fe: 320.466 mg	Fe: 321.488 mg	Fe: 319.034 mg	Fe: 322.298 mg
Co: 338.638 mg	Co: 336.054 mg	Co: 338.034 mg	Co: 338.814 mg	Co: 338.452 mg
Ni: 348.000 mg	Ni: 344.174 mg	Ni: 347.500 mg	Ni: 348.044 mg	Ni: 346.410 mg

2.2.MJ CrCoNi

Standard weight amounts:

Cr: 307.690 mg Co: 347.104 mg Ni: 345.205 mg

MJ CrCoFe-1	**MJ CrCoFe-2**	**MJ CrCoFe-3**	**MJ CrCoFe-4**	**MJ CrCoFe-5**
Cr: 306.690 mg Co: 346.674 mg Ni: 345.634 mg	Cr: 305.210 mg Co: 347.442 mg Ni: 344.510 mg	Cr: 310.198 mg Co: 348.616 mg Ni: 349.616 mg	Cr: 307.292 mg Co: 344.882 mg Ni: 344.460 mg	Cr: 309.400 mg Co: 348.054 mg Ni: 348.400 mg

These samples were then collected in designated containers with the name of the resultant alloy.

3.3 Arc Melt Furnace:

In this step, the metal pieces were arc melted to form a single alloy. For this purpose an arc melt furnace machine was used. It consisted of a copper base with depressions in it for the collection of the sample metals. The metal pieces were collected in these depressions with a Titanium ball in the middle. These are then placed in an air tight container and vacuum is created in this chamber with the help of a suction pump in order to prevent oxidation at the surface of the alloy. Once a good vacuum pressure of 10^{-6} mbar is achieved, we can perform our experiment. An arc is generated inside the container and its direction is controlled with the help of a probe. First the Titanium ball placed in the centre is melted in order to check its solidification. If no oxidation is evident in that ball, we can proceed with the alloy making process.

Figure 21 Arc Melt Furnace

The alloys are provided with the arc and since they have a higher affinity with each other rather than the aluminum plate, they form a ball and an equiatomic alloy is produced. As the desired result is to achieve proper solidification without oxidation, Argon gas is used to cool the chamber

down. Once this is done (and there are no signs of oxidation on the sample) our sample is ready to use for the next step.

These steps were performed for both the High Engineering Alloys and High Entropy Alloys as well.

3.4 Electromagnetic Lavitation

This is the most important step of the entire process. Electromagnetic Levitation is a method by which an object is suspended with no support other than the electric and magnetic fields. These forces are used to counteract the effects of the gravitational acceleration and any other acceleration. It is possible with this process for electrically conductive samples to be solidified container-free. The experimental unit consists of a vacuum receiver with pumping system, a high frequency generator, an oscillator, a copper coil, a temperature measuring unit and a gas supply system.

In our apparatus, a copper coil is placed inside a container with a pump attached to it for creating vacuum. The design of the coil is such that it allows for opposing magnetic forces in the centre while allowing for current to pass through it for heating purposes. A ceramic tube is placed vertically in the centre of the coil, our sample is placed on this ceramic tube and air is pushed through this tube to propel the sample in the middle of the coil. Before this however, we have to close our container and achieve a vacuum of 10^{-6} mbar is applied and then backfilled with Argon to Atmospheric pressure. Once the sample is in the middle, the opposing magnetic forces help to keep the sample stable in the middle and the electric forces induced inside the sample because of the magnetic effects help in increasing the temperature. A high speed camera with a 7000 frames per second recording speed is placed in front of the sample in order to record the melting and cooling of the sample and a laser is placed on the sample in order to measure the

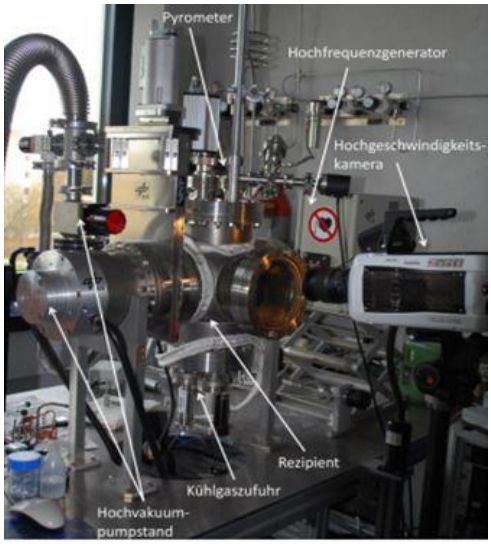

Figure 22 Electromagnetic Levitation Machine

temperature changes which are being recorded in a graph in the software. The sample is melted and the molten liquid is kept levitated in order to avoid solidification due to contact with any exterior surface. The molten sample is cooled slowly and the recalescence is observed through the high speed camera which indicated undercooling and is shown by a vertical dip in the temperature graph. This process can be repeated a few times and the undercooling can be studied. After this the samples were placed under argon and continuous cooling melted together. The samples were weighed after being solidified by EML to make sure that the mass loss was less than 1.5%.

Samples were solidified with various undercooling values using electro-magnetic levitation technique. For levitation in the EML samples were thus with a mass of 1 g weighed. During the entire reflow, the temperature, and the solidification rate, is measured with an Infrared Pyrometer. The shape of the Freezing front during hypothermia is recorded with the aforementioned high-speed camera. The Figure shows a schematic temperature-time profile. Several such cycles can be repeated for a single sample. The temperature measurements from the pyrometer can be calculated from the formula given below:

$$\frac{1}{T} = \left(\frac{1}{T_{Pyr}}\right) + \left(\frac{1}{T_L}\right) - \frac{1}{T_L^{Pyr}}$$

This event is visible in the temperature profile as a temperature gradient jump between melt and solid as a bright front on the sample surface are recorded with the high-speed camera.

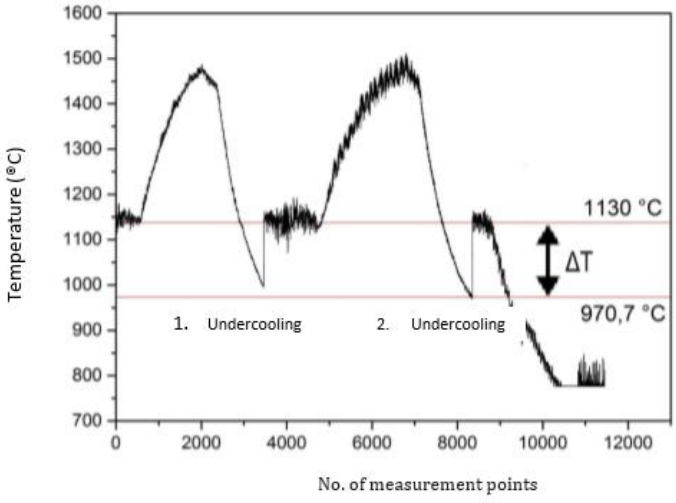

Figure 23 Cooling Curve

3.5 Grinding, Polishing and Microscopy:

After the undercooling is done, we cut our sample in half to get a semi spherical sample; the rounded side of this sample is then mounted with the help of a hot press in the Bakelite powder in order to make the handling of the sample easier. Once this is done, the samples are grinded

and then polished with the help of basic OPS solution in order to make the viewing of the microstructure easier. Grinding started with a 1000 grit paper up to a 4000 grit paper, cleaned in the ultrasonic bath and finally with ethanol. After this the sample was polished with alumina (0.05 μm). The polishing is done with a suspension of aluminum slurry, move the sample round and round and perform even cleaning, so that the liquid does not stick to one end only. After this remove the dirt and clean the sample with the help of Acetone. Use the 9.8 basic SiO_2 suspension (clean with acetone on top so as to avoid damages caused by agglomerates) to further clean the sample.

Once the sample was polished, we inspected it with the help of an optical microscope in order to visualize its dendrite structure. To observe the microstructure, LEO1530 scanning electron microscope (SEM) was utilized. Back scattered electron detector (BSE) was also used to investigate the microstructure, electron back scattered diffraction (EBSD) to determine the grain orientation and energy dispersive spectroscopy (EDS) has been utilized to find out the composition of different phases present in the samples. We observed that in our sample there was a coarse dendrite structure in the centre. A reason for this could be that the structure started its cooling from the outside so there was very fine structure on the outer surface, and started getting coarser in the middle and therefore the big porosity.

3.6 SEM

The last step of our process was to perform SEM on our sample. Some clean gas (Argon or Nitrogen) was pumped into the chamber in order to open the chamber, so we can lace the sample. The tip of the gun is polished with Zirconia to assist the movement of electrons without producing too much heat and thereby keeping the beam narrow (1.2 – 1 nanometer), and a tungsten tip is present to accelerate the electrons.

Once the sample is placed inside the chamber, we induce vacuum into the chamber. As the vacuum increases, the mean free path of the rouge atoms inside also increases more than the size of the chamber and so it keeps moving around like billiard ballsnever actually going inside the small diameter hole of the gun chamber. No particle should be allowed to go inside the gun chamber because it could deflect the path of the electron. The electron beam should remain sharp

and narrow for better resolution. The E.H.T turns on electron accelerator, the maximum voltage is 100 V, and we focus on the low magnification so that large area is covered. We use a working distance (distance between lens and specimen) is 15 units. With the help of this we get a clearer image of the sample microstructure. The direction of the grains can be color coded to give us a more comprehensive picture of our samples.

3.7 Micro Vicker:

The mechanical property of a material can be studied by analyzing its ability to withstand load. For this purpose, various hardness tests are performed to measure the capacity of a structure to bare a certain amount of load on different scales.

For the study on Ni Sn Alloy and its different microstructures, nano and micro level indentation technique was opted to be the best way forward.

3.8 Nano Indentation:

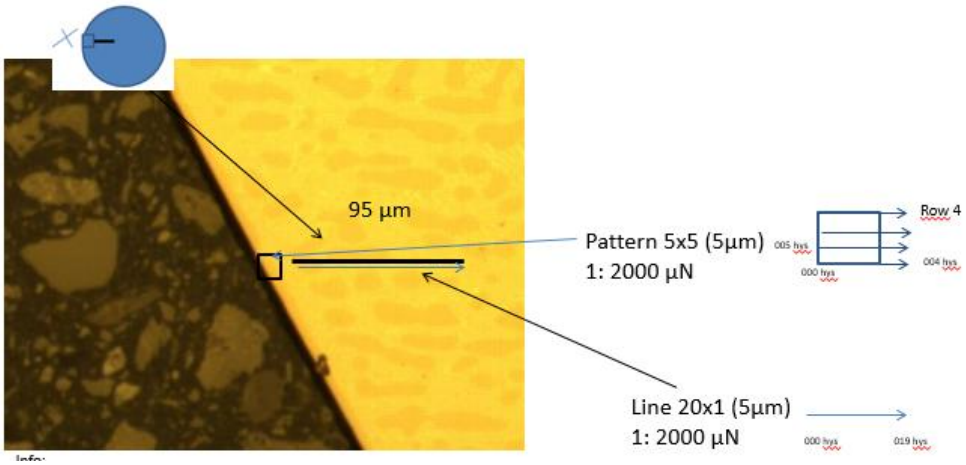

Figure 24 For sample with undercooling approx. 20K

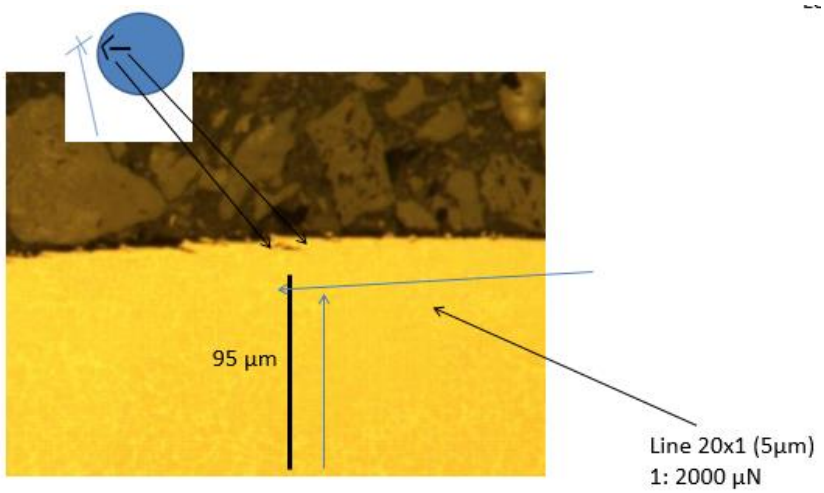

Figure 25 For sample with undercooling approx. 165 K

Chapter 4: Results

4.1 Cooling Curves:

The relevant part of the Ni-Sn phase diagram is shown in Fig. 1. The alloy composition used for the study is shown with a red line. Equilibrium solidification of such a composition starts at around 1150°C with the formation of pro-eutectic Ni3Sn phase. As the Ni3Sn phase grows, the remaining liquid decrease in Ni content. At 1132°C, the remaining liquid has the eutectic composition of 32.5 wt. % Sn and solidifies as α-Ni- Ni3Sn lamellar. During the melting and solidification process, temperature is constantly measured and plotted to give characteristic cooling curves; one of them being shown in Fig below.

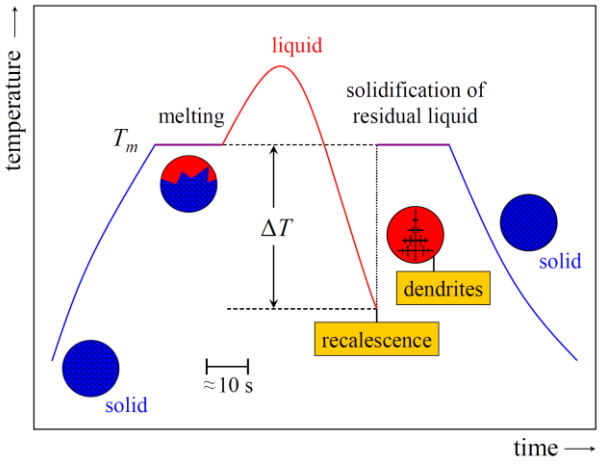

Figure 26 Cooling Curves of Undercooled samples

As the sample is heated up, it first undergoes a solid-solid phase transformation where

hexagonal Ni3Sn is transformed into cubic phase of the same composition. As the temperature is further increased, melting of the sample takes place at around 1150°C.

It is supposed to solidify at the same temperature where it started to melt; however, due to absence of any container walls, it experiences an undercooling of around 115°C. Once the entire sample is solidified, the temperature starts to drop down with one slight increase when solid state transformation takes place for the Ni3Sn phase.

.

4.2 Crystal Growth Velocity

Rapid growth of dendrites is a crucial dynamic solidification behavior during rapid solidification of the undercooled alloy. Crystal growth velocities for the NiSn samples have been plotted against undercooling in the Fig.

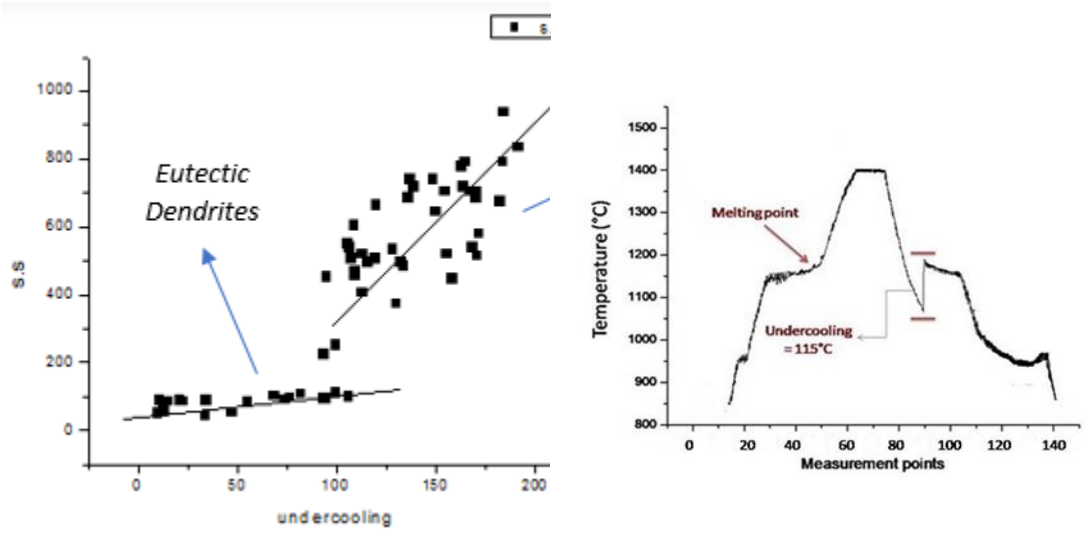

Figure 27 showing trend of growth velocity with change in undercooling:

As by changing undercooling values it varies many properties like can see from graph, by increasing undercooling value, solidification speed also increases gradually.

4.3 Microstructural Evolution:

The results of the SEM done on the samples are given below:

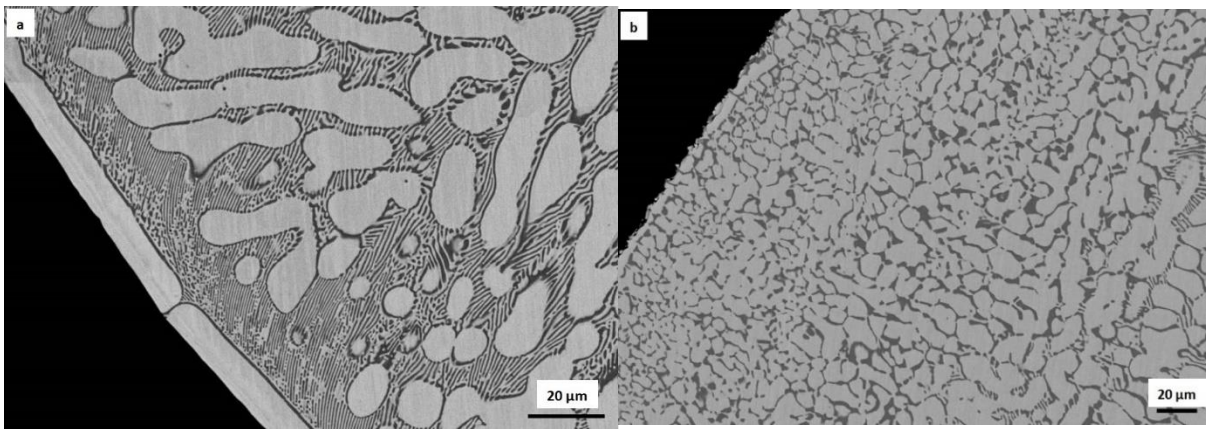

Figure 28 Microstructure of Ni-Sn hyper-eutectic alloy after solidification at a) 20K and b) 140K

:

The microstructures of both NiSn samples with different undercooling values are shown in Fig. We can see there is a visible difference between the microstructure of the sample at different undercooling values. In the figure a, the sample was undercooled at a value of 20 K and this shows a structure having lamellar present, at this low value of undercooling. For the low undercooling, the microstructure consists of pro-eutectic Ni3Sn phase and lamellar eutectic of α-Ni phase and β Ni3Sn intermetallic compound.

In figure b, we observe that at large value of undercooling that is of 140 K shows the presence of non-lamellar microstructure means one phase present in the matrix of other. We can observe the non-lamellar eutectic is present towards the edge of the sample while lamellar eutectic can be towards the center of the sample.

The α-Ni phase appears dark while the β Ni3Sn appears bright in the microstructure shown in Fig.

4.4 Solidification Front:

In the following fig, the different solidification fronts that occurred during the solidification of the hyper-eutectic Ni-Sn alloy are presented. The solidification fronts recorded with the high-speed camera shows difference with difference in undercooling values.

For high undercooling value, the solidification speed is so high that it doesn't show the diffusion while more characteristic solidification fronts appear. At low undercooling value, the samples solidify on the one side with diffusely growing on the surface, shown in Figure b as an example.

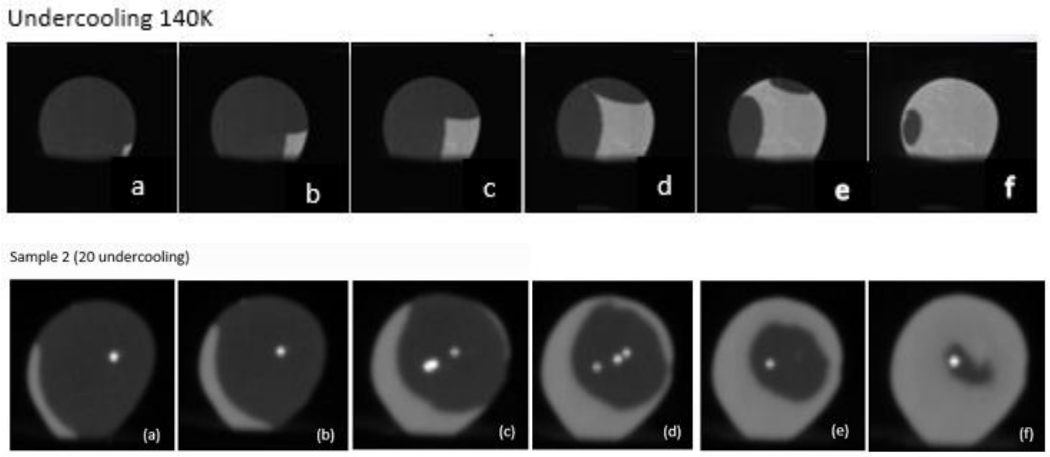

Figure 29 Showing difference of recalescence front during solidification of melt at high and low undercooling

4.5 Nano Indentation:

Nano indentation has been proven to be essential in determining the contribution of Ni rich phase and the NiSn3 Intermetallic phase present in the lamellar as well as the non-lamellar structure found in the alloy. The nanohardness results shows that the intermetallic phase has a hardness lower than the Ni rich phase (Lamellar) which can be due to the presences of grain boundaries that, in abundance, hinder the movement of dislocation due to any stress applied making the alloy harder as clearly stated by R. Imayev and G. Salishchev in their paper that the microstructure of the alloys tend to have a great impact on its property and is governed more by the grain boundaries than the grain size. This shows that more grain boundaries tend to create more hinderance for the movement of dislocations, over all making the alloy exhibit higher hardness values.

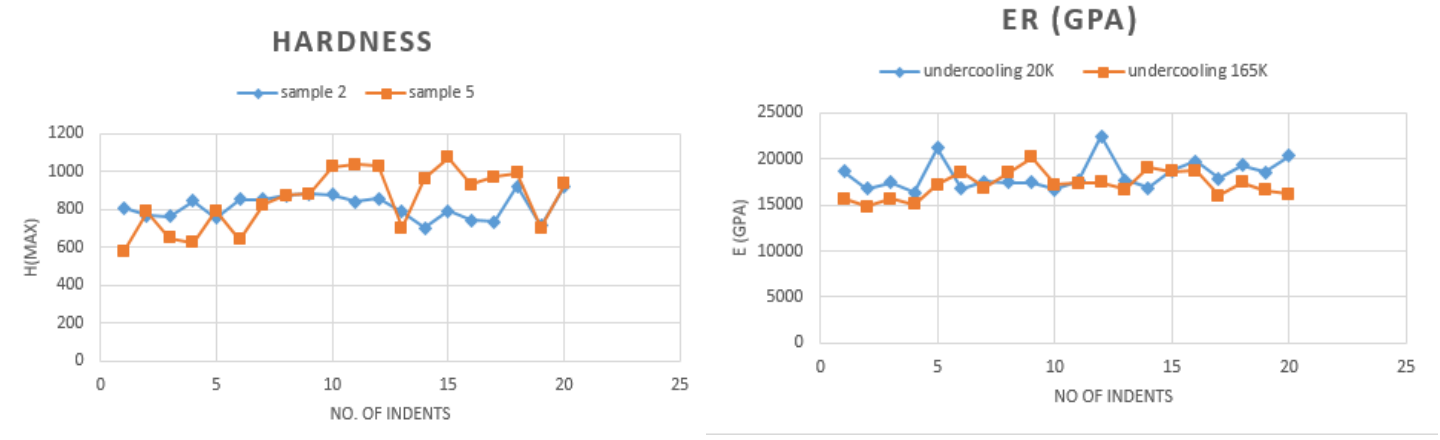

Figure 30 rend of hardness and elastic modulus at high and low undercooling values

Nano hardness has helped figure out the roles of the two different phases in the alloy while the micro hardness test further confirmed the previously gained results.

4.6 Micro-Vickers:

Here is the result of micro Vickers hardness test done on NiSn samples undercooled at different ranges. Discussing about the physical characteristics of solidification behavior, the growth

velocity of dendrites has a great influence on the mechanical properties of the alloy. This mechanical behavior changes are mainly because of grain refinement and microstructural evolution caused because of the rapid dendritic growth.

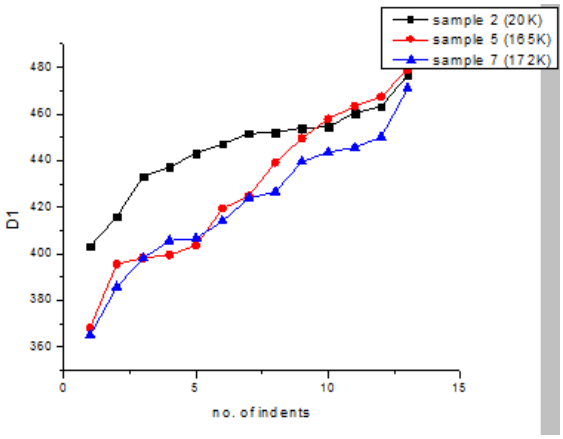

This graph is showing trend of undercooling with hardness. As Undercooling value increases the hardness value also decreases.

Figure 31 Graph shows the trend of Vickers hardness at different undercoolings

4.7 XRD:

Here are the results for XRD for two different samples having different undercooling values.

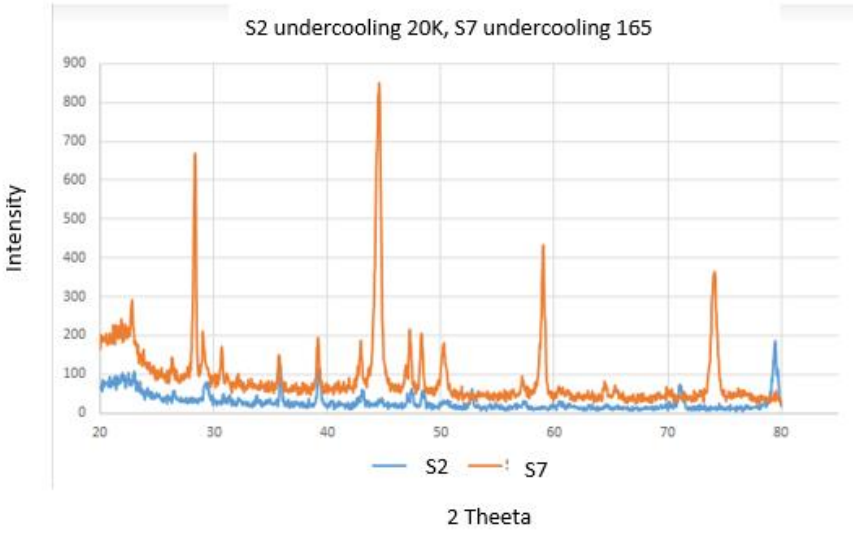

Figure 32 Comparison of XRD peaks of high and low undercooling

Chapter 5: Discussion

The main objective of this thesis is to investigate the microstructure of the eutectic alloy Ni813Sn187 as a function of supercooling in crucible-free processing. One focus is on the better understanding of the origin of the anomalous eutectic, as described by Gao et al[19] was investigated for this alloy. Growth rates were measured and the microstructure examined by means of SEM, EDX and EBSD. In the following, the results of this investigation will be presented and discussed. In addition, EML samples with hyper-eutectic compositions were produced, also melted free of crucibles and supercooled. The results contribute to a better understanding of the formation of the non-lamellar eutectic and are also included in the discussion.

5.1 Time Temperature Profile:

A series of samples was solidified with supercooling from near equilibrium up to $\Delta T = 170K$. A sample was melted several times and the temperature-time profile recorded each time, as well as the solidification front filmed. After several cycles, the sample was saved and the microstructure examined. Figure 27 shows an example of such a temperature-time profile with two cycles.

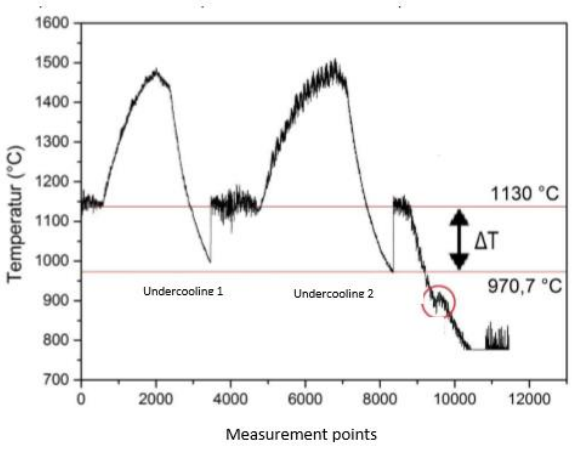

Figure 33 Time temperature profile for NiSn obtain from pyrometer

In the region of the eutectic equilibrium temperature, a short plateau is formed in which the solid and the melt are in equilibrium before the temperature rises further. The amount of supercooling of the melt cannot be influenced and therefore assumes different values for each cycle. After Recalescence the temperature jumps back to the eutectic equilibrium temperature, again passes through a plateau and can then either rise again by adjusting the gas flow or flatten further. At 900 ° C, a short increase in temperature can be observed. The rise in temperature is much smaller here than in the solidification, which indicates a solid-state transformation already described by Schmetterer et al.[10] was described.

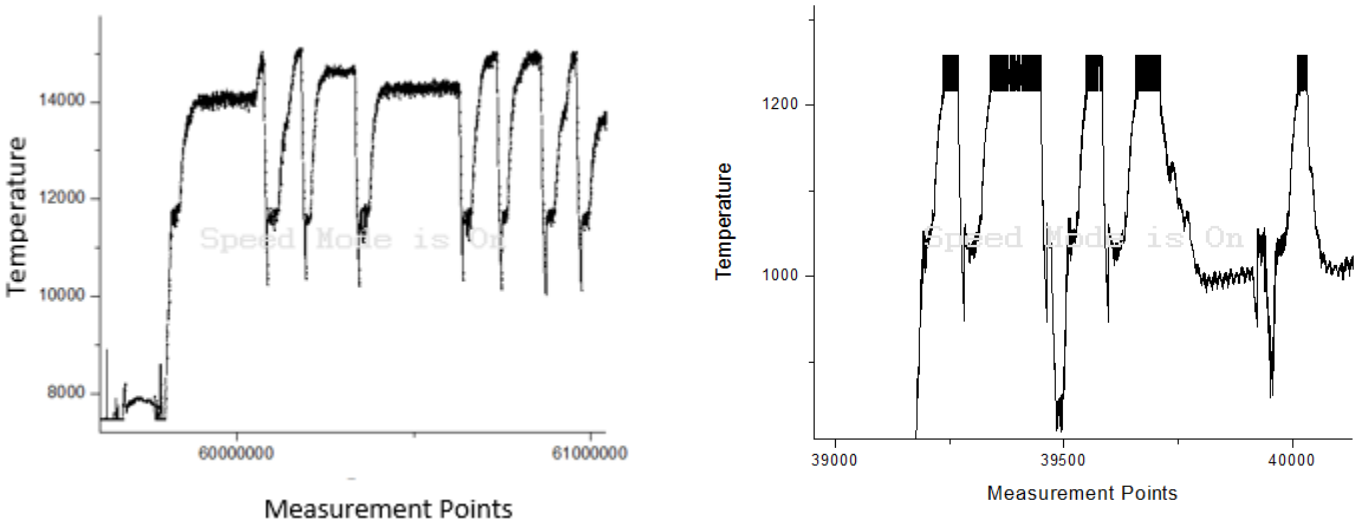

Figure 34 Several cycles of undercooling shown in Time temperature profile of NiSn for (a) high undercoolings (b) low undercoolings

5.2 Solidification Speed:

The solidification rates were determined from the recorded high-speed videos, as described earlier, and plotted against undercooling. Error can also exist there; the high inaccuracy of measurement is also reflected in the scattering of the data points for the respective undercooling temperatures as can be seen in figure 21. Nonetheless, the data points show a general trend that is consistent with previous work [11, 20] on this NiSn system. The curve shows a speed increase

from around ΔT = 120 K. This result agrees very well with the measurements of Gao et al.[22] who also observed an increase in velocity in this temperature range for the same alloy composition.

Some basic parameters of dendritic growth like velocity and tip radius corresponded with the undercooling (deltaT). Considering the non-equilibrium effect, the connection between dendritic growth and undercooling can be described as,

$$\Delta T = \Delta Tt + \Delta Tc + \Delta Tr + \Delta Tk + \Delta Tn$$

Where thermal undercooling is ΔTt, ΔTk is the kinetic undercooling, ΔTr is the curvature undercooling and ΔTn is the undercooling that is caused by altered equilibrium liquidous. The total change in undercooling due to solute contribution is called solutal undercooling ΔTc.. These are different types of undercooling on which our results dependent.

Whenever we have a slow solidification process, for eutectic alloys, at first, one phase nucleates then the second phase nucleates dependently on the first phase, which results in the formation of a lamellar structure. However, in the case of fast solidification, the results would be different than those mentioned above. This can be explained by using the TMK eutectic growth and LKT/BCT dendritic growth theories that can help explain the eutectic and dendritic growth velocities.

In our case the growth velocity increases suddenly when undercooling exceeds proximately 120 K, as from literature the growth velocity rises abruptly at higher undercooling value from nearly 3 ms−1. This is likely related to the kinetic-controlled growth also affected by the compositional changes in liquid and solid phase present[2, 3]. Further increase in undercooling value approx. 447K, the growth velocity of (αFe) dendrites approaches a plateau. In the case of pure Ni and Ni-Cu alloy, such a dendritic-growth-velocity plateau is recognized to the effect of residual oxygen that serves as an additional solute[4, 5]

This increase in our system is also explained by Gao et al. based on two different solidification mechanisms for the areas of small and large undercoolings. For small undercooling values, up to

ΔT = 120K, eutectic dendrites grow after that at higher undercooling Ni-rich dendrites grow as shown in Figure 21. The eutectic dendrite is characterized by cooperative, diffusion-controlled growth of the nickel-rich phase α and the Ni3Sn β phase, exemplified in Figure 29.

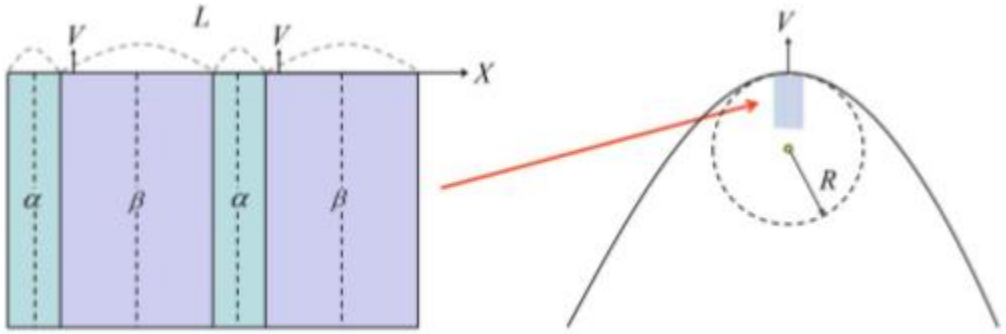

Figure 35 Schematic showing lamellar eutectic growth of dendrites

This lamellar growth is slower than the growth of pure metals or single-phase alloys in supercooled melts. Measurements can be found in Kobayashi et al.[21].

When higher supercooling is achieved, the mechanism of solidification changes and nickel-rich dendrites grow primarily. Overall, however, the rates for primarily growing, pure nickel dendrites are not reached by the nickel-rich dendrites growing here [16]. The reason for this is the proportion of dissolved tin atoms in the nickel phase. As the dendrite grows into the melt, in addition to the nickel atoms, tin atoms must also be incorporated into the crystal structure of the solidifying phase, which slows growth.

5.3 Grain Growth:

The investigations to date on samples of the eutectic composition to crystal growth rate, change of the microstructure towards higher undercooling, the orientation of the individual grains and the shape of the solidification front, brought some insight into the formation of the anomalous eutectic, but raised new questions, such as Existence of the eutectic dendrite.

In order to better understand some mechanisms, therefore, samples with a near eutectic composition were prepared. If the concentration of one of the two elements is increased, the associated phase is formed preferentially. More nickel means preferential growth of the nickel-rich dendrite. More tin in the system leads to an increased formation of the intermetallic Ni3Sn phase. Each sample was undercooled for several cycles and the microstructures observed at the end.

The respective solidification fronts at low undercooling values were spherical and without prominent areas. This suggests the solidification of many dendrites in different growth directions from the nucleation point. Such a front is shown as an example in Figure 30.

The dendrite grows primarily from the melt, partially melts and breaks. The resulting fragments served as germinal sites for the growing microstructure. Even in the liquid melt these are swirled around and solidify therefore in the different orientations.

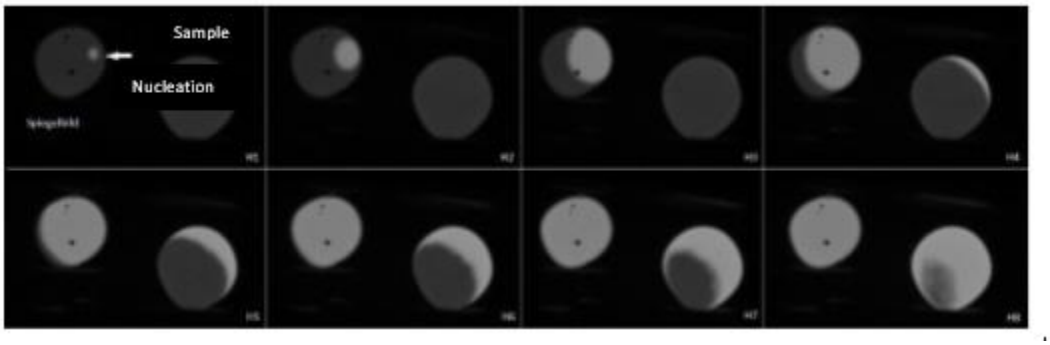

Figure 36 Recalescence front at low undercooling value.*:*

Tin rich samples and can be transferred to the fine-grained regions in the eutectic samples with high undercooling. Another observation, in the context of this work, was made at the solidification front of the tin-rich phase. In contrast to the nickel-rich phase, no spherical solidification front is formed. A prominent solidification front was observed on the sample surface, Figure 31 shows an example of such a front at high undercooling.

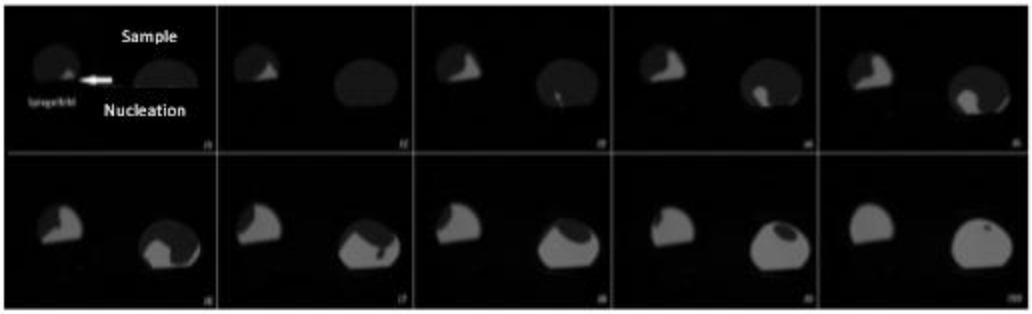

Figure 37 Recalescence front at high undercooling value

In this case, it has been possible to determine the geometry of the crystal growing here. Figure 32 shows the modeling of the front. The solidification front could be exactly reproduced, the geometry of the solidifying crystal are derived from it.

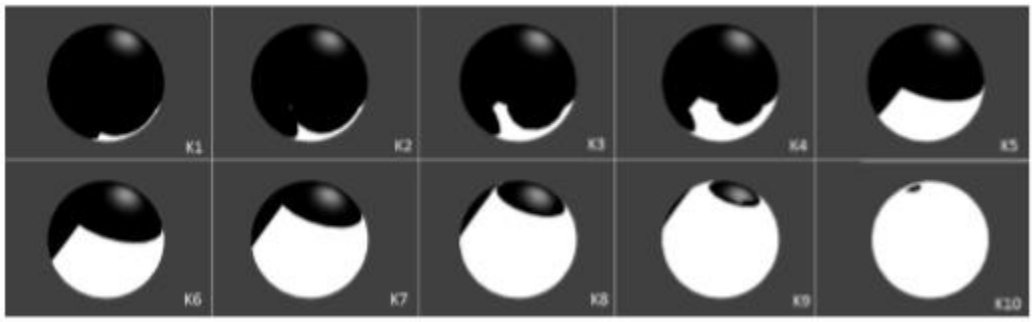

Figure 38 Model for the reproduction of the solidification front. The underlying geometry of the crystal can be deduced from this. In this case, a distorted octahedron.

This was based on a distorted octahedron. The perforation of the dendrite tips that span the octahedron give the shape of the solidification front. This octahedron can be found in one of the crystal structures proposed by the literature [8] for the high-temperature phase of the Ni3Sn phase. The Cu3Ti structure is a cubic crystal structure, in which, however, six-fold structures can be found. These hexagonal structures, in turn, are well suited for conversion to the hexagonal low-temperature phase of Ni3Sn. An atomic model of this crystal structure is shown in Figure 33. The atomic distances are registered in the Angstrom unit.

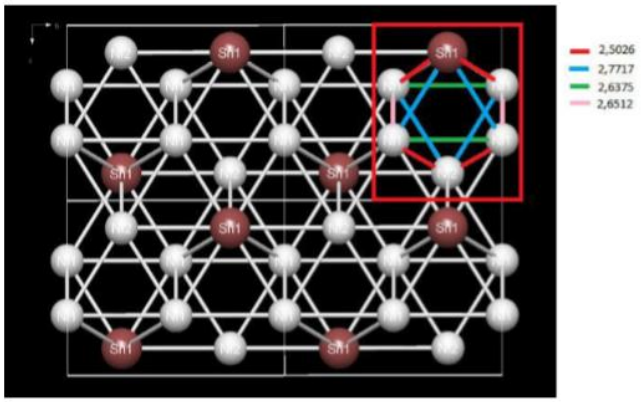

Figure 39 : Atomic model of the Cu3Ti structure, which was found to be a solution for the crystal structure of the high-temperature phase of the Ni3Sn phase. The model was created with the program Diamond.

For a better illustration, Figure 34 shows a detailed view of the octahedron in the crystal structure. The octahedron is drawn in red. A tin atom (Sn1) and a nickel atom (Ni2) form the tips of the octahedron. Four more nickel atoms (Ni1) sit on the other corners. The two pyramids, which together form the octahedron, are identical, only the four lateral surfaces of the respective pyramid have different sizes, since the side edges of the pyramids have different lengths.

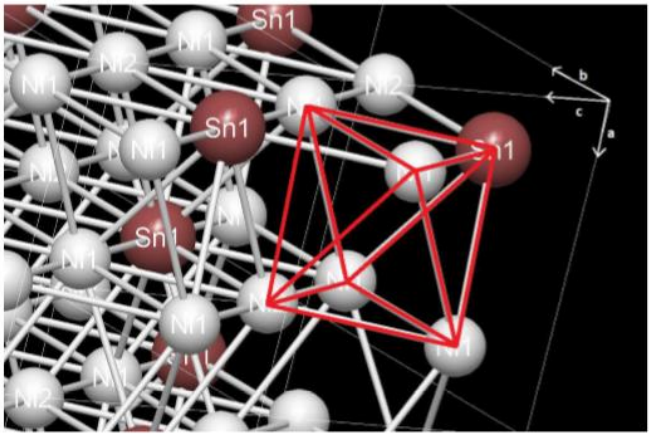

Figure 40 Detailed view of the octahedron as found in the crystal structure of Ni3Sn. The octahedron is drawn in red.

This leads to the conclusion that the observed solidification front can be assigned to the high-temperature phase of the Ni3Sn phase. To clarify is still how the orientation of the nickel-rich phase fits this geometry. Based on the assumption that the nickel-rich phase epitaxially grows on

the crystal structure of the high-temperature phase of the Ni3Sn phase, the six main directions found in the nickel-rich phase would have to be correlated with the identified octahedron. The six tips of the octahedron lend themselves to this attempt as they pick up the six directions. As a rule, however, phases grow on surfaces.

5.3.1 Investigation of The Solidification Front:

Not only the microstructure or the orientation of the solidifying grains can provide conclusions on the solidification front, also released during solidification heat of fusion and the associated increase in temperature can be observed on the sample surface and provide information about the underlying process.

As described in 5.3, the crystal growth rate can be determined by observing the solidification front across the sample surface. The solidification front shows the intersections of the solidifying crystalline body with the sample surface, wherein the change in the solidification front reflects the growth of the solidifying body by the sample volume. To uniquely determine the growth rate of a crystallographic direction, the geometry of the solidifying crystal must be known. A spatial analysis of the shape and location of the dendrites in the melt, which span the growing crystal, is required to make more accurate statements. The structure of the growing crystal can be derived from the contact points with the sample surface. Marked points of contact, for example, represent a growing dendrite peak. As shown in Figure 35, a dendrite that grows along the <100> direction in a cubic crystal system evolves into a regular octahedron, with six main directions and perpendicularly growing secondary dendrite arms. [12]

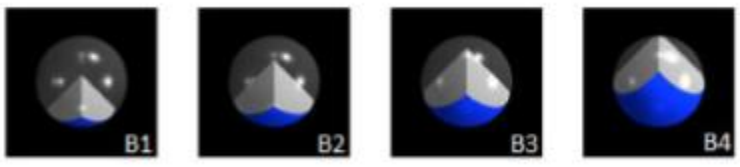

Figure 41 Dendrites that grow in the six spatial directions of the cubic crystal lattice span a crystal with the geometry of a regular octahedron.

The crystal growth rate can then be deduced from the geometry of the growing crystal. Figure 36 shows the schematic nucleation of a dendrite at a point on the surface, which then grows along a preferential direction into the melt. Growth in the preferred direction is complete once the dendrite tip re-pierces the sample surface (B4). At this time, some areas of the sample are still liquid. However, the remaining time to solidify these areas should not be considered when determining the crystal growth rate.

Figure 42 Schematic representation of an octahedral crystal growing through the liquid sample. The blue area shows the intersection of the crystal with the sample surface. The light gray body is the part of the crystal that solidifies below the surface.

For this simple geometry, a determination of the crystal growth rate is possible because the high-speed recordings of the solidification front in the EML and EBSD measurements of the microstructure help us to recognize the crystal morphology and to create geometric models by means of suitable programs. Solidifying more complex geometric bodies, or multiple crystals simultaneously in the sample, can be seen in the high-speed videos. In this case, a derivative of the crystal structure from the shape of the solidification front is difficult to impossible. In addition, arbitrary orientations of the preferred directions, within the liquid phase, influence the shape of the solidification front, so that it requires many images of the same alloy system with constant experimental parameters until the geometry of the crystal can be determined. Computer-aided three-dimensional models can help with this process, Figure 36. In the following, the different solidification fronts that occurred during the solidification of the eutectic Ni-Sn alloy are presented and discussed. The solidification fronts recorded with the high-speed camera can

be divided into three types. For low undercooling, the samples solidify on the one hand with diffusely growing nucleates on the surface, shown in Figure 37 as an example.

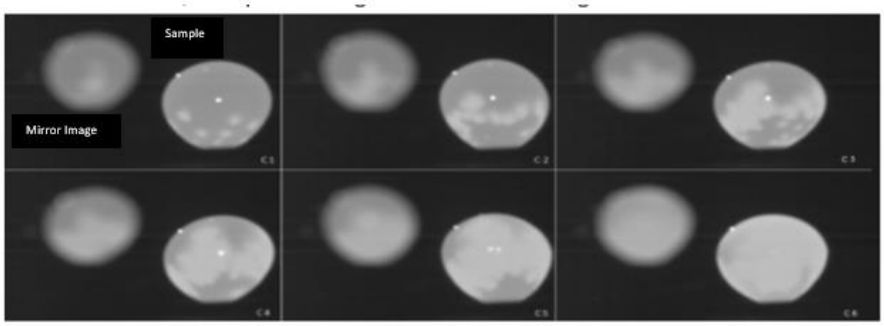

Figure 43 Schematic representation of an octahedral crystal growing through the liquid sample at low undercooling

The solidification rate is in the range of a few cm / s and the geometric orientation of the crystal can not be deduced from this front. The left image is the mirror image, the right image is the sample.

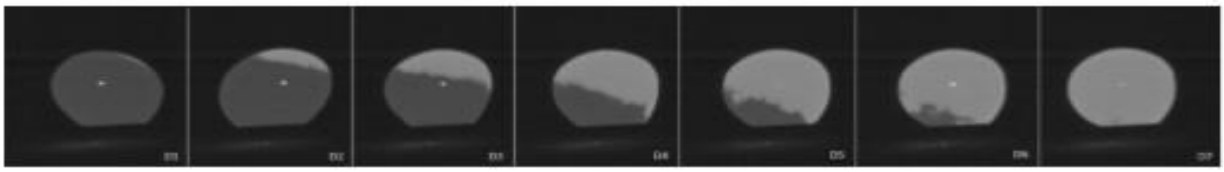

Figure 44 Schematic representation of an octahedral crystal growing through the liquid sample at undercooling 110K.

Spherical fronts are believed to be spanned by many dendrites that grow in different directions simultaneously, as illustrated in Figure 39. The jagged course of the front is caused by single dendrites breaking through the surface at these points.

The appearance of two different solidification fronts for small undercooling could be an indication of two different mechanisms of solidification that occur here. Since the shape of the dendrites is no longer visible in the microstructure analysis and based on the solidification front no model for the growing crystal geometry could be derived, these mechanisms are not explicable in the context of this work.

In the range of high undercooling above $\Delta T = 100K$, more characteristic solidification fronts appear. Shortly after onset of solidification, the solidification front shows a multitude of four-

cornered or hexagonal formations. During solidification, the front becomes coarse again, as in the samples with smaller undercooling.

In the course of further solidification, some other samples also produced distinctive features on the solidification front, which may give indications of the solidifying geometry, as shown in Figure 40.

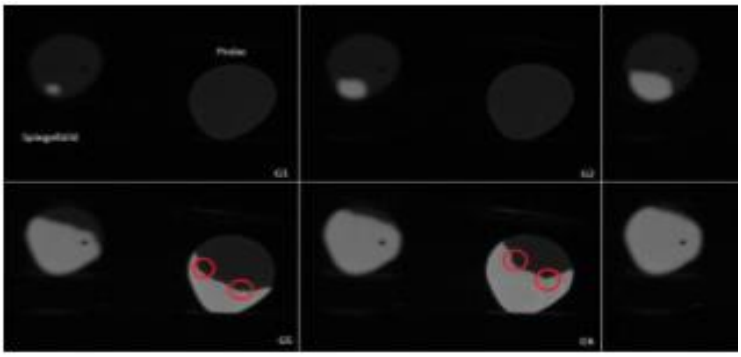

Figure 45 Schematic representation of several dendrites growing from the nucleation point at different angles into the melt.

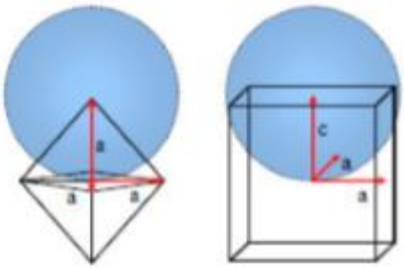

Figure 47 The left image is the mirror image of the sample, the right image the real image of the sample. The solidification front has some distinctive features, marked in red in pictures G5-G8.

The shape of the front in Figure 36 points again to dendrites growing from the nucleation point in different directions into the melt. Gao et al. Assumes the primary growth of the nickel-rich dendrite

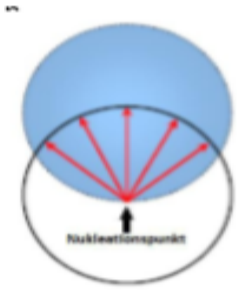

Figure 46 Model for propagating an octahedron or cuboid in a sphere to simulate the shape of the solidification front taken with the high-speed camera.

or high supercooling. Whether these solidification fronts are due to the growth of the nickel-rich dendrite, or whether the Ni3Sn phase solidifies here, could not be conclusively clarified. On the one hand, there are currently no scientific papers on the individual solidification fronts of the nickel-rich phase or the intermetallic phase Ni3Sn. On the other hand, as already discussed, investigations of the microstructure at the SEM did not provide any further information. The Ni3Sn phase experiences a solid-state transformation and is therefore no longer present in its originally solidified form. The nickel-rich dendrite is fragmented into many small pieces. For further clarification, independent

experiments, for solidification from the supercooled melt, at the nickel-rich phase and the Ni3Sn phase would be necessary. Considerations of the solidification fronts of the individual phases could provide conclusions about the present geometry of the crystal.

Dendritic microstructure is the main microstructural constituent formed during the solidification process of an alloy. Due to high undercooling rapid, dendritic growth occurs by the rapid movement of solid interface in liquid melt. The Recalescence times for both hypoeutectic and eutectic alloys decrease rapidly with increasing undercooling. From the result, we see that the formation of dendrites for low and high undercooling values is different, for high undercooling we see a sharp dendritic formation while for low values coarse dendrites form. We can find in literature, recalescence takes place in two stages: first, dendrites sweep across the sample, resulting in rapid recalescence; and second, coarsening takes place, resulting in slow recalescence.

The tip of the dendritic radius experiences a large difference of temperature, this results in rapidly grown dendrites. This phenomenon of dendritic growth formation in undercooled melt can be explained by the marginal stability theory derived from Ivantsov paper [3]and microscopic solvability theory considering interfacial free energy[4-7] from the growth models described by harvay and Cahn[14]. Theoretical models to further understand this concept have been developed by many investigators, beginning with that of Langer and Muller-Krumbhaar.[12]

To study the interaction in detail there exists many reliable experimental techniques used to quantitatively measure the velocity of dendrite with change in undercooling. In this we used Electromagnetic Levitation technique to achieve undercooling for our alloy, the sample is levitated and at the same time is heated by the eddy currents. No external heating source is required in this process. Other container-less solidification techniques which are commonly employed are drop tube solidification, electro-static levitation (ESL) and aero-dynamic levitation (ADL), Glass fluxing etc and feasible to achieve high undercooling values with low cooling rates. The details about these techniques can be found in literature [8, 19]

This repaid dendritic growth results in the grain refinement and hence the altered mechanical properties of alloy. The grain refinement contribution to the improved mechanical properties of Fe-based alloys (especially for the hardness) is well established in the literature[16-18]

5.4 Microstructure:

The analysis of the microstructure was carried out on SEM images of the halved samples, using EDX spectroscopy and EBSD. The purpose of the EDX analysis was to check the chemical composition of the levitated samples in order to ensure that the desired eutectic composition was achieved. This was the case in all the samples available. On the other hand, the two existing phases were characterized. In the following backscatter images taken in the SEM, the dark phase is the cubic surface centered, nickel-rich phase, the light phase is the hexagonal intermetallic Ni3Sn phase.

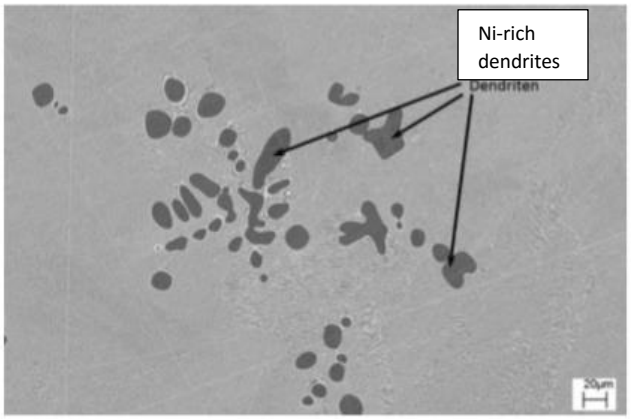

Figure 48 Equilibrium solidification, single nickel-rich dendrites grow and are surrounded by normal lamellar eutectic.

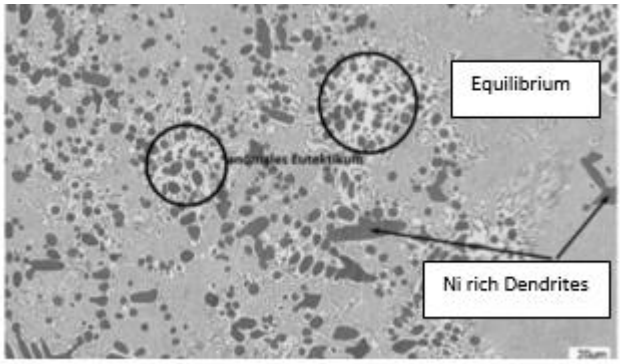

Figure 49: It is a series of experiments Dedicated to the local equilibrium eutectic, as well as single anomalous eutectic colonies

First, SEM images were taken of samples with different undercooling. An overview is shown in Figures 41-47. Overall, an increase in the anomalous eutectic towards higher undercooling is evident. Figure 41 shows the microstructure of a solidified sample. In fine-lamellar equilibrium eutectic some nickel-rich dendrites have formed. This indicates a slight over-concentration of nickel in this sample.

Figure 42 shows the microstructure of a sample with low supercooling. On display are many dendrites of the nickel-rich phase. In the interstices of the dendrites continues to form

equilibrium eutectic. In some places, here marked with circles, colonies of anomalous eutectic begin to form. The nickel-rich phase and the Ni3Sn phase grow cooperatively as small grains and no longer alternately as light and dark lamellae. At the margins of these colonies either single nickel-rich dendrites form or a transition to lamellar equilibrium eutectic takes place.

In Undercooling ΔT = 85K-150K form colonies of abnormal eutectic. These colonies are still surrounded by equilibrium eutectic, shown in Figure 42. With increasing hypothermia, the colonies of anomalous eutectic become larger. At the edges of the colonies, individual nickel-rich grains coarsen. If 150K supercooling is exceeded, there is anomalous eutectic throughout the sample, as shown in Figure 43

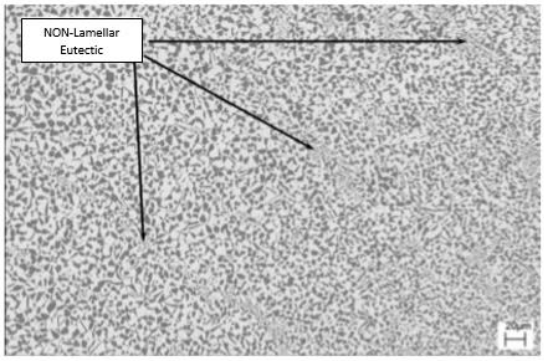

Figure 50 Sample at ΔT = 190 K, form colonies of non-lamellar eutectic. In addition, nickel-rich dendrites grow.

Occasionally, both the nickel-rich phase and the Ni3Sn phase are embedded in globular morphology in the equilibrium eutectic. Presumably, occasionally growing nucleates are responsible for this, which form in the eutectic melt. The intermetallic Ni3Sn phase occurs less frequently. This suggests that in the present system for the nickel-rich phase, there is less nucleation work and nickel-rich nuclei can be more easily formed.

On the basis of the photographs 41-47 shown, a development of the microstructure as a function of the supercooling can be observed, as described by Gao et al. was observed. In the range of small undercooling up to T = 40K, equilibrium eutectic forms, in which sparingly nickel-rich dendrites grow. From T = 40K to T = 150K, dendrites of the nickel-rich phase and the intermetallic Ni3Sn phase are formed first, and then colonies of anomalous eutectic grow. From T = 150K the samples are essentially anomalous eutectic. Dendrites grown in spherical morphology are no longer observed.

For areas with large nickel-rich grains, Gao et al. as a mechanism of the growth of a nickel-rich dendrites, this grows at high undercooling primarily from the melt and then breaks. The resulting

fragments serve as nucleation sites for the nickel-rich grains. The result is a grain-fined microstructure. The formation mechanism for the areas of the small grains could not be sufficiently clarified on the basis of the EBSD measurements. Since a preference orientation can be recognized in the XRD plots, a different generation mechanism must be assumed, compared to the large grains. Also by Gao et al. proposed for this purpose, the growth of a eutectic dendrite, as soon as the melt comes close to equilibrium temperature during the recalescence. This eutectic dendrite also fragments and serves as a nucleation site for the fine grain areas. A complete, eutectic dendrite was not found in any of the samples studied.

In conclusion the microstructure of low undercooling hypereutectic NiSn consists lamellar eutectic of α-Ni and β-Ni3Sn intermetallic compound. For moderate undercooling in the range of 140-150 K, we observe that the observation of the proeutectic Ni3Sn phase occurs first at high velocity; whereas the remaining liquid present in that area does not get enough time to diffuse into the lamellar structure and concentrates as the α-Ni phase and therefore solidifies at that

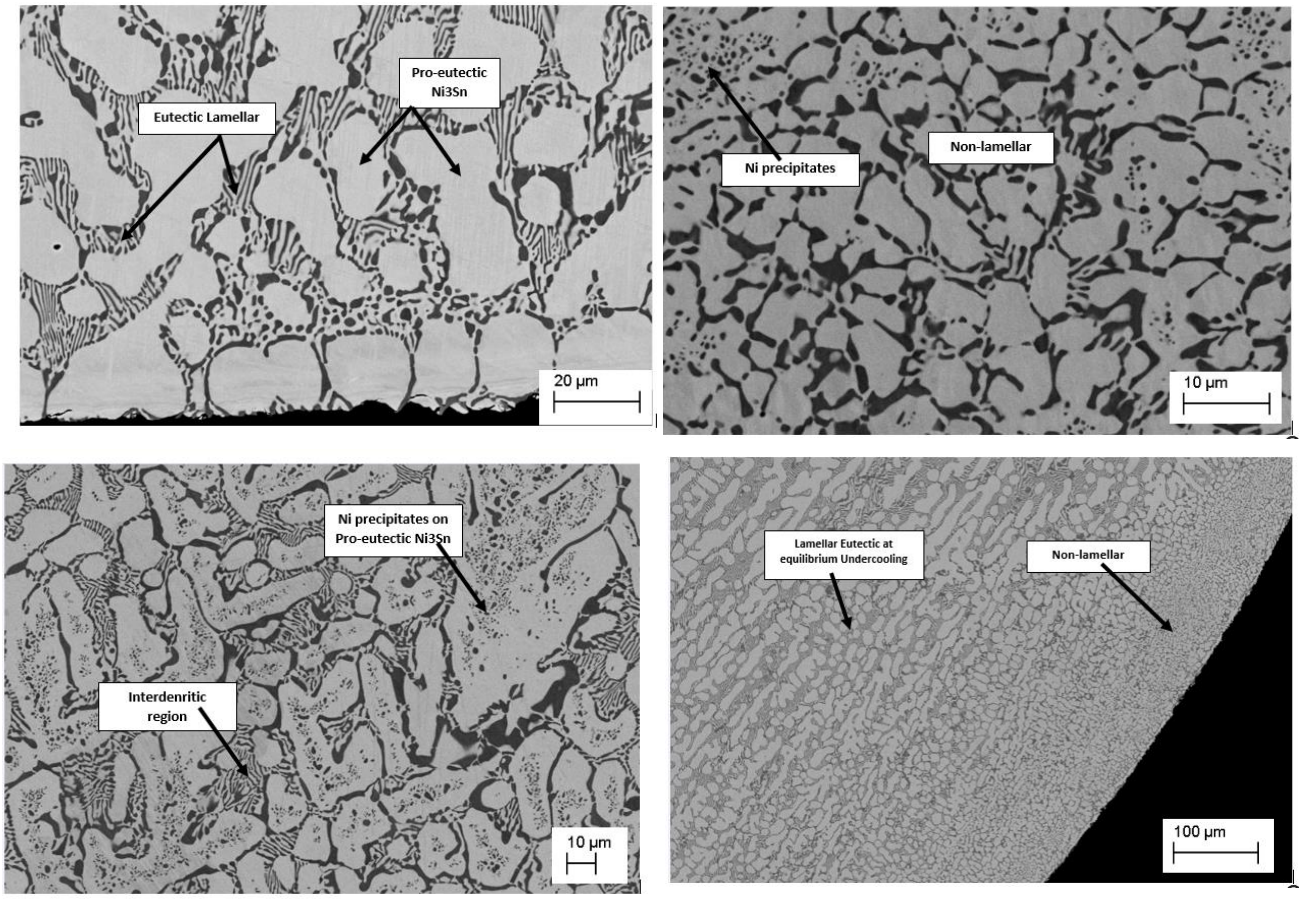

Figure 51 : SEM images at different undercoolings showing variation in structures.

point. We can say that the arrangement that we observe of both of the phases in the Lamellar Structure, is different from the arrangement in the non lamellar eutectic, rather in this case one phase precipitates out onto the other. This is because Argon gas is used in the chamber for cooling purposes which reduces the heat present in the surface and causes it to solidify more quickly as compared to the centre. Once the temperature reaches the melting point, the remaining liquid has now more time to arrange themselves so they diffuse giving us the lamellar structure in the centre.

Therefore we can say that at the areas of equilibrium solidification we get a lamellar eutectic phase and those areas where the solidification was rapid, and after a certain critical value, the microstructure changes. For even higher values of undercooling, in the range of 160-170 k, it appears at first that the eutectic dendrites of α-Ni and β-Ni3Sn intermetallic compounds is created, but as the temperature moves towards the melting point, this initially created eutectic phase melts(as the temperature increases that of the melting point of the eutectic phase) and creates the proeutectic Ni3Sn dendrite and the remaining α-Ni that was present in the eutectic phase could have been precipitated out onto the proeutectic dendrites.

As from literature we see that for hypo eutectic compositions the microstructure changes in the same manner. At lower degree of recalescence we get regular eutectic structure, at moderate we get anomalous zones and lamellar zones and then at values greater than 130K, only anomalous phase is present.

5.5 Variation with Hardness:

5.5.1 Nano Indentation:

Nano indentation has been proven to be essential in determining the contribution of Ni rich phase and the Ni3Sn Intermetallic phase present in the lamellar as well as the non-lamellar structure found in the alloy. The nanohardness results shows that the intermetallic phase has a hardness lower than the Ni rich phase (Lamellar) which can be due to the presences of grain boundaries that, in abundance, hinder the movement of dislocation due to any stress applied making the alloy harder as clearly stated by R. Imayev and G. Salishchev in their paper that the microstructure of the alloys tend to have a great impact on its property and is governed more by the grain boundaries than the grain size. This shows that more grain boundaries

File	Pmax(µN)	hmax(nm)	Er(GPa)	H(GPa)
S2 line 2 0000 LC.hys	2000	88,42	186,34	8,10
S2 line 2 0001 LC.hys	2000	92,41	167,53	7,67
S2 line 2 0002 LC.hys	2000	92,18	174,49	7,64
S2 line 2 0003 LC.hys	2000	88,82	163,50	8,45
S2 line 2 0004 LC.hys	2000	89,83	211,87	7,57
S2 line 2 0005 LC.hys	2000	87,93	167,34	8,53
S2 line 2 0006 LC.hys	2000	87,28	175,09	8,52
S2 line 2 0007 LC.hys	2000	86,17	174,52	8,72
S2 line 2 0008 LC.hys	2000	85,78	174,07	8,83
S2 line 2 0009 LC.hys	2000	87,16	166,39	8,76
S2 line 2 0010 LC.hys	2000	87,65	175,77	8,42
S2 line 2 0011 LC.hys	2000	83,43	224,38	8,59
S2 line 2 0012 LC.hys	2000	90,61	176,83	7,88
S2 line 2 0013 LC.hys	2000	96,40	168,13	7,03
S2 line 2 0014 LC.hys	2000	89,03	186,82	7,92
S2 line 2 0015 LC.hys	2000	91,85	197,29	7,43
S2 line 2 0016 LC.hys	2000	93,64	178,52	7,35
S2 line 2 0017 LC.hys	2000	82,10	192,66	9,24
S2 line 2 0018 LC.hys	2000	94,29	185,41	7,16
S2 line 2 0019 LC.hys	2000	81,69	202,90	9,23

File	Pmax(µN)	hmax(nm)	Er(GPa)	H(GPa)
S5 line 2 0000 LC.hys	2000	107,03 €	156,78 €	5,77 €
S5 line 2 0001 LC.hys	2000	93,24 €	148,11 €	7,90 €
S5 line 2 0002 LC.hys	2000	101,37 €	156,85 €	6,51 €
S5 line 2 0003 LC.hys	2000	104,03 €	150,97 €	6,24 €
S5 line 2 0004 LC.hys	2000	90,83 €	172,04 €	7,91 €
S5 line 2 0005 LC.hys	2000	99,35 €	185,08 €	6,41 €
S5 line 2 0006 LC.hys	2000	89,81 €	168,06 €	8,23 €
S5 line 2 0007 LC.hys	2000	85,53 €	184,39 €	8,73 €
S5 line 2 0008 LC.hys	2000	83,76 €	201,77 €	8,80 €
S5 line 2 0009 LC.hys	2000	80,27 €	171,40 €	10,24 €
S5 line 2 0010 LC.hys	2000	79,78 €	173,70 €	10,36 €
S5 line 2 0011 LC.hys	2000	80,15 €	174,35 €	10,27 €
S5 line 2 0012 LC.hys	2000	96,95 €	167,12 €	7,01 €
S5 line 2 0013 LC.hys	2000	81,16 €	190,75 €	9,64 €
S5 line 2 0014 LC.hys	2000	77,38 €	186,23 €	10,74 €
S5 line 2 0015 LC.hys	2000	82,91 €	187,34 €	9,30 €
S5 line 2 0016 LC.hys	2000	83,73 €	159,56 €	9,70 €
S5 line 2 0017 LC.hys	2000	81,29 €	174,19 €	9,90 €
S5 line 2 0018 LC.hys	2000	96,39 €	166,09 €	7,04 €
S5 line 2 0019 LC.hys	2000	84,74 €	161,53 €	9,36 €

Figure 52 Nano-hardness data shown for sample with undercooling of 165K

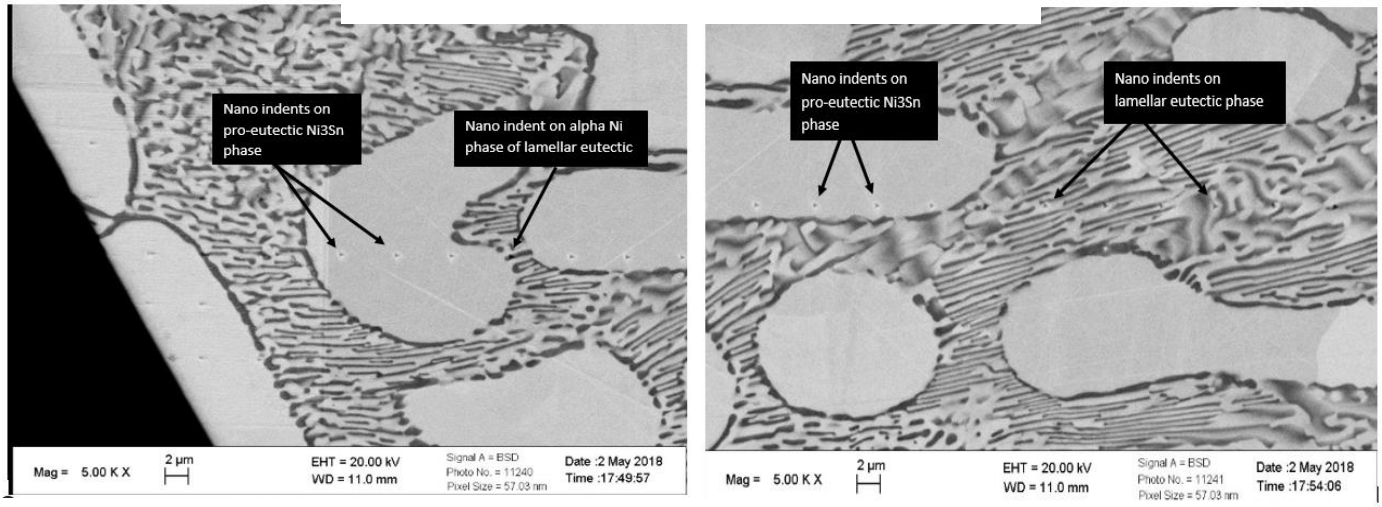

Figure 53 Nano-indents can also be clearly seen in some SEM images in.

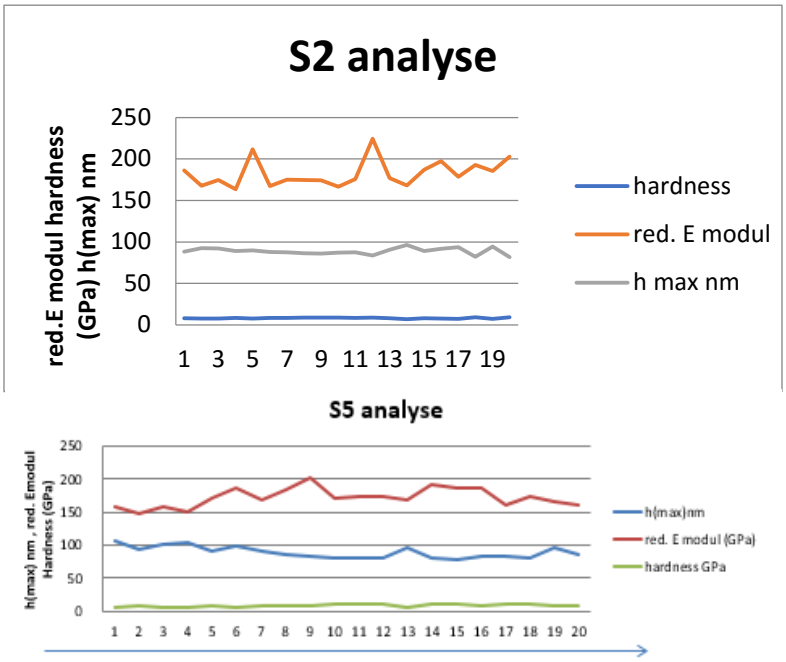

Figure 54 Nano-hardness data shown for sample with undercooling of 20K

5.5.2 Micro Indentation:

The microhardness for alloy samples solidified at higher undercooling have less lamellar structure and more non -lamellar structures consisting of randomly oriented NiSn3 and Ni rich phase. Alloys with such structure gave low micro hardness values as the amount of lamellar structure for very low. On the other hand, alloy samples cooled at lower undercooling had the favorable conditions to solidify in an almost equilibrium pattern resulting in large areas consisting of lamellar phase. These samples had higher hardness values confirming the nano hardness results.

As discussed in "Microstructural and Mechanical Property Manipulation through Rapid Dendrite Growth and Undercooling in an Fe-based Multinary Alloy" by Y. Ruan, A. Mohajerani & M. Dao, the increase in Grain boundaries has affected the mechanical properties of the alloy as it refined the grains. If a comparison is done, the lamellar structure would always have more grain boundaries than the intermetallic contributing to the high hardness values of the alloy.

Nano and micro hardness both showed that the undercooling increase leads to lower hardness of the alloy. The lamellar phase contributes higher value of hardness than the intermetallic due to the abundant grain boundaries in it. All in all, the undercooled structure has less lamellar structure which results in lower hardness of the alloys.

5.6 XRD Analysis:

At an undercooling range of 20 – 150 K, we observe two phases in our XRD analysis. One phase is of the FCC phase α – Ni and hexagonal phase Ni3Sn which are the same as the equilibrium phases. From literature, we see that in the hypo composition in an undercooling range of 380K, the Ni – 32.5 wt% Sn alloy in its XRD showed the presence of the peaks of the same two phases, In our result, we observed that as we increase the undercooling of the samples, the peaks present in the analysis reduces in number.

This can be explained by the directionality (textured) of the grains, at higher values of undercooling the grains have more directional properties. This is because at higher undercooling, the solidification speed is high and so the grains are not allowed to settle in their preferred manner. Therefore we can say that by decreasing the equilibrium conditions the directionality of the grains increases and this leads to lower number of plains diffracting the XRD beams and hence smaller number of peaks in the result.

5.7 Comparison with HEA:

Crystal growth velocities for the NiSn and HEA samples have been plotted against undercooling in the Fig. 48 and are compared with literature values of pure Ni growth.

As expected, the solidification speed for the NiSn samples has been found to be the slowest at all undercooling values. It is because intermetallics have more ordered structure and more time is required for the formation of ordered lattice during the solidification process. In case of pure metal, the solidification speed is the fastest as no lattice ordering is required. In case of HEAs, the solidification speed is faster than that of hyper-eutectic NiSn but slower than that of pure Ni. As HEAs mostly consist of disordered solid solutions, the solidification process is not slowed down due to ordering. However, as there are atoms of different sizes present in the mixture, the diffusion is slower. Also, the interaction between atoms of different species is different. For example in case of NiCoCrFeCu, Cu tends to separate from Co, Cr and Fe resulting in a 2 phase microstructure. This also slows down the solidification speed when compared with a pure metal.

5.8 Hardness Comparison with HEA:

High entropy alloy possesses numerous variables that control its properties. The hardness of these alloys can be lower than advance engineering alloys such as NiSn for several reasons. The elemental types, the percentage lattice distortion and the type of structures the solid solution of these elements form.

The alloy NiCoFeCrCu contains two different phases both with FCC structure that encourages the dislocation movement making it softer than NiSn

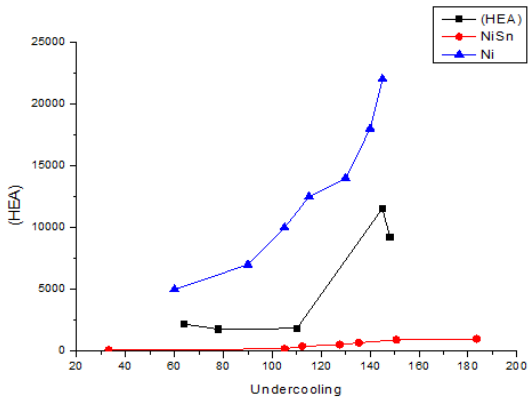

Figure 55 Solidification speed vs undercooling for the NiSn, HEA and pure Ni.

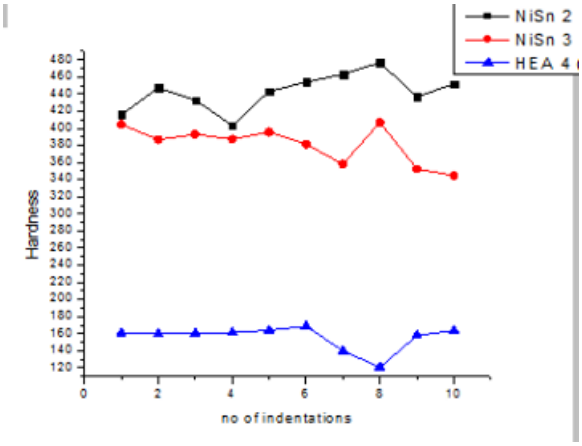

Figure 56 showing the comparison of hardness of Ni-Sn and High Entropy Alloy

5.9 Microstructure Analysis of HEA

Microstructure of an undercooled high entropy alloy of composition NiCoCrFeCu has been shown in Fig. 49. It shows dendritic morphology with Cu-lean dendritic phase and inter-dendritic

Cu-rich phase. The two-phase microstructure of this high entropy alloy is due to presence of Cu which tends to separate from Co, Cr and Fe [8]. Both the phases have FCC crystal structure with Cu- rich phase having lattice parameter of 0.36148nm and Cu-lean phase showing lattice parameter of 0.35859nm. Till date, no one has solidified this composition using electro-magnetic levitation technique, however, solidification by glass fluxing showed a reduction in the volume of Cu-rich phase with increasing undercooling and its convergence by forming Cu-rich spheres. In the present study, NiCoCrFeCu HEA has been solidified with undercooling values up to 150K, however, some SEM measurements are still pending to have a better comparison with the results from glass fluxing experiments.

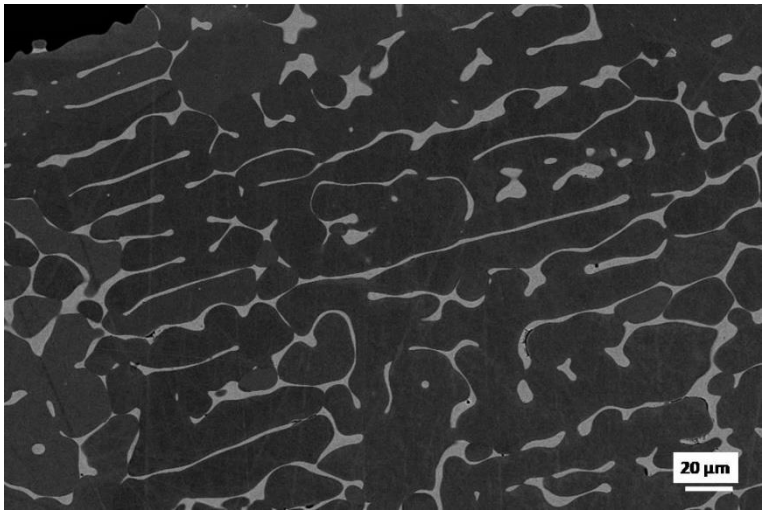

Figure 57 Microstructure of Ni-Co-Cr-Fe-Cu high entropy alloy solidified with an undercooling of 60K

Chapter 6: CONCLUSION

In the present work the formation of anomalous eutectic was observed for the alloy nickel + Ni3Sn. For this purpose, samples were melted without container and solidified with different undercooling in the range of nearly equilibrium solidification up to ΔT =250 K. The solidification front was recorded and the microstructure of the samples was subsequently examined by means of EDX and EBSD.

Undercooling of ΔT = 150K initially formed colonies of anomalous eutectic, whose volume fraction in the sample increases with increasing undercooling. For high undercooling above ΔT =150 K, only non-lamellar eutectic is present in the samples.

The formation of this non-lamellar eutectic was reported by Gao et al. already presented two theories. For the area of small undercooling, growth and subsequent fragmentation of a eutectic dendrite are assumed. To high undercooling then grows primarily a nickel-rich dendrite, which breaks and melts. At the same time, the eutectic dendrite, which is fragmented, is also forming for other areas. This eutectic dendrite can grow as the residual melt nears the eutectic temperature during the recalescence. The respective fragments serve as nucleating sites for the resulting non-lamellar eutectic.

The measured crystal growth rates confirm this theory and are in good agreement with those of Gao et al. carried out measurements.

For low undercooling, no theory for the development of the anomalous eutectic could be provided in this work. It has been shown that the nickel-rich phase solidifies in various orientations without strong texture, while the Ni3Sn phase is in the form of a few large grains. The underlying mechanism was not clarified. Also a eutectic dendrite was not found in any of the samples.

Investigations of the intermetallic Ni3Sn phase showed the influence of the solid state transformation in the range of 900 ° C. A cubic high-temperature phase converts to a hexagonal crystal structure at room temperature. The orientation of the nickel-rich grains remains unaffected by this transformation as evidenced by orientation measurements across grain boundaries of the Ni3Sn phase.

In order to better understand the solidification mechanism of the individual phases, nickel-rich and tin-rich samples were prepared and also processed in the EML. The nickel-rich samples show a highly grain-fined microstructure with a regular texture, formed by a fragmented, nickel-rich dendrite.

The tin-rich samples solidify in dendritic morphology in the intermetallic high-temperature Ni3Sn phase, with nickel-rich precipitates in the center of these regions. These nickel-rich precipitates also solidify in the six directions already found in the eutectic samples and are unaffected by the orientation of the cryogenic Ni3Sn phase.

Investigations of the solidification front of these tin-rich samples have shown that a striking solidification front can be observed on the sample surface. The geometry of the solidifying crystal could be modeled as a distorted octahedron.

It has been shown that the present orientation of the nickel-rich phase remains unaffected by the solid state transformation in the original orientation of the high temperature phase of the Ni3Sn phase. The high-temperature phase of Ni3Sn can probably be assumed to be the Cu3Ti structure. The geometry of the solidifying crystal of the Ni3Sn phase was identified as a distorted octahedron. This octahedron is also found in the Cu3Ti structure. To explain the correlation between the orientations of the nickel-rich phase and the crystal structure of the Ni3Sn phase, epitaxial growth of the nickel-rich phase to the Ni3Sn-intermetallic phase is assumed. The eight octahedral surfaces serve as the basis. However, not all surfaces are equivalent due to the distortion of the octahedron, so that only six surfaces serve as nucleation sites. The Ni3Sn phase primarily solidifies before the nickel-rich phase can grow on the crystal surfaces.

The existence of eutectic dendrites could not be clarified. For samples with eutectic composition it was not observed in any sample. The present micrographs of the tin-rich sample can be interpreted as dendritic fragments, which were surrounded and conserved in their morphology by

a growing Ni3Sn phase. In the present case, however, it may also be merely nickel-rich precipitates from the supersaturated Ni3Sn phase.

Nano and micro hardness both showed that the undercooling increase leads to lower hardness of the alloy. The lamellar phase contributes higher value of hardness than the intermetallic due to the abundant grain boundaries in it. All in all, the undercooled structure has less lamellar structure which results in lower hardness of the alloys.

From XRD analysis we obtained that at higher undercooling, the solidification speed is high and so the grains are not allowed to settle in their preferred manner. Therefore, we can say that by decreasing the equilibrium conditions the directionality of the grains increases and this leads to lower number of plains diffracting the XRD beams and hence smaller number of peaks in the result

Concluding this work, container-less solidification of eutectic and high entropy alloys has been carried out and the effect of undercooling on solidification speed, microstructure and recalescence behavior have been investigated. From the preliminary results, following conclusions could be drawn.

1. Undercooling values up to 150K for both NiSn and NiCoCrFeCu alloys can be achieved using electromagnetic levitation technique.
2. Solidification of hyper-eutectic NiSn alloy with low undercooling values results in dendrites of pro-eutectic β-Ni3Sn phase with inter-dendritic lamellar phase of α-Ni and β-Ni3Sn.
3. With increasing undercooling anomalous eutectic of α-Ni and β-Ni3Sn starts to form.
4. The solidification speed of NiSn alloy has been found to be 5-10 times slower than the NiCoCrFeCu high entropy alloy.
5. Microstructure of NiCoCrFeCu HEA consists of Cu-lean dendritic phase and Cu- lean inter-dendritic region.

Chapter 7: Attachments

GRAPHS DATA

Sample 2 20k undercooling	*Sample 5 165k undercooling*	*Sample 7 172k undercooling*
476.7	368.3	365.1
463.2	395.7	385.8
460.5	398.3	398.2
454.5	399.6	405.7
454	403.6	406.6
452.2	419.5	414.1
451.6	424.9	423.9
447.2	439.2	426.6
443.2	449.6	439.6
437.2	457.9	443.6
433.2	463.4	445.7
415.9	467.4	450.1
403.2	479	470.9
445.585 Avg	*428.185 Avg*	*421.223 Avg*

Table 1

Undercooling	Speed	Undercooling	Speed	Undercooling	Speed
9.0	280.00	112.0	525.06	157.4	451.61
10.0	411.76	112.2	411.81	162.3	783.01
10.0	262.50	114.8	500.00	163.2	721.86
10.0	283.78	118.4	512.21	164.1	796.52
10.0	91.70	119.0	669.57	167.0	710.75
33.0	47.47	122.8	855.59	168.0	543.52
33.7	94.94	127.6	537.20	169.6	689.58
58.4	133.33.	129.3	378.38	170.0	519.11
93.0	228.71	131.4	770.04	170.0	710.75
94.0	457.41	133.1	488.60	170.9	584.80
99.0	256.41	135.4	689.58	181.5	679.43
105.0	556.63	136.3	745.17	183.0	796.52
105.1	200.00	138.2	721.86	183.4	942.86
105.7	545.45	147.9	745.17	191.1	840.02
106.8	512.82	149.0	650.70		
107.0	871.74	150.7	923.98		
108.0	607.90	154.0	710.75		
108.6	477.33	154.5	525.03		
108.6	461.54	154.7	525.03		

Table 2

Chapter 8: References

1. Porter, D.A., K.E. Easterling, and M. Sherif, *Phase Transformations in Metals and Alloys, (Revised Reprint)*. 2009: CRC press.
2. Herlach, D.M., *Non-equilibrium solidification of undercooled metallic melts.* Metals, 2014. **4**(2): p. 196-234.
3. Herlach, D.M. and D.M. Matson, *Solidification of Containerless Undercooled Melts*. 2012: John Wiley & Sons.
4. Yao, W., N. Wang, and B. Wei, *Containerless rapid solidification of highly undercooled Co-Si eutectic alloys.* Materials Science and Engineering: A, 2003. **344**(1-2): p. 10-19.
5. Wu, Y., et al., *Dendritic growth of undercooled nickel-tin: Part I.* Metallurgical and Materials Transactions A, 1987. **18**(5): p. 915-924.
6. Wu, Y., et al., *Dendritic growth of undercooled nickel-tin: Part II.* Metallurgical and Materials Transactions A, 1987. **18**(5): p. 925-932.
7. Wu, Y., et al., *Dendritic growth of undercooled nickel-tin: Part III.* Metallurgical Transactions A, 1988. **19**(4): p. 1109-1119.
8. Powell, G. and L. Hogan, *UNDERCOOLING IN SILVER-COPPER EUTECTIC ALLOYS. PT. 1. NUCLEATION. PT. 2. MICROSTRUCTURE.* INST METALS J, 1965. **93**(14): p. 505-512.
9. Kattamis, T. and M. Flemings, *Structure of undercooled Ni-Sn eutectic.* Metallurgical and Materials Transactions B, 1970. **1**(5): p. 1449-1451.
10. Yang, C., et al., *New evidence for the dual origin of anomalous eutectic structures in undercooled Ni–Sn alloys: in situ observations and EBSD characterization.* Acta Materialia, 2011. **59**(10): p. 3915-3926.

11. Bassler, B., W. Hofmeister, and R. Bayuzick, *The solidification velocity of pure nickel.* Materials science and Engineering: A, 2003. 342(1-2): p. 80-92.
12. Wei, B., et al., *Rapid dendritic and eutectic solidification of undercooled Co‧Mo alloys.* Materials Science and Engineering: A, 1994. 181: p. 1150-1155.
13. Yeh, J.W., et al., *Nanostructured high-entropy alloys with multiple principal elements: novel alloy design concepts and outcomes.* Advanced Engineering Materials, 2004. 6(5): p. 299-303.
14. Zhang, Y., et al., *Microstructures and properties of high-entropy alloys.* Progress in Materials Science, 2014. 61: p. 1-93.
15. Otto, F., et al., *Relative effects of enthalpy and entropy on the phase stability of equiatomic high-entropy alloys.* Acta Materialia, 2013. 61(7): p. 2628-2638.
16. Jones, B., *Growth mechanisms in undercooled eutectics.* Metallurgical and Materials Transactions B, 1971. 2(10): p. 2950-2951.
17. Bingbo, W., Y. Gencang, and Z. Yaohe, *High undercooling and rapid solidification of Ni‧32.5% Sn eutectic alloy.* Acta metallurgica et materialia, 1991. 39(6): p. 1249-1258.
18. Li, J., et al., *Enhanced mechanical properties of a CoCrFeNi high entropy alloy by supercooling method.* Materials & Design, 2016. 95: p. 183-187.
19. Guo, T., et al., *Liquid-phase separation in undercooled CoCrCuFeNi high entropy alloy.* Intermetallics, 2017. 86: p. 110-115.
20. Belin-Ferre, E., *Basics of thermodynamics and phase transitions in complex intermetallics*. Vol. 1. 2008: World Scientific.
21. Bazant, Z.P., *Thermodynamics of solidifying or melting viscoelastic material.* ASCE J Eng Mech Div, 1979. 105(6): p. 933-952.
22. Flemings, M.C., *Solidification processing.* Metallurgical transactions, 1974. 5(10): p. 2121-2134.
23. Jena, A. and M. Chaturvedi, *Phase transformation in materials*. 1992: Prentice Hall.

24. Frank, F.C., *Supercooling of liquids.* Proc. R. Soc. Lond. A, 1952. **215**(1120): p. 43-46.
25. Hunt, J. and K. Jackson, *Binary eutectic solidification.* Transactions of the Metallurgical Society of AIME, 1966. **236**(6): p. 843-&.
26. Górny, M., *Solidification of thin wall ductile iron castings with hypereutectic composition.* ISIJ international, 2010. **50**(6): p. 847-853.